

**ANNUAL REPORT ON**

**APPLICATION OF MODEL-BASED SIGNAL  
PROCESSING METHODS TO COMPUTATIONAL  
ELECTROMAGNETICS SIMULATORS**

**Office of Naval Research  
Research Grant N00014-98-1-0178**

**For the period December 1, 1997 through November 30, 1998**

**Submitted by**

**Professor Hao Ling**

**Department of Electrical and Computer Engineering  
The University of Texas at Austin  
Austin, TX 78712-1084**

**December 15, 1998**

**19981229 027**

# REPORT DOCUMENTATION PAGE

Form Approved

OMB No. 0704-0188

Public reporting burden for this collection of information is estimated to average 1 hour per response, including the time for reviewing instructions, searching existing data sources, gathering and maintaining the data needed, and completing and reviewing the collection of information. Send comments regarding this burden estimate or any other aspect of this collection of information, including suggestions for reducing this burden to Washington Headquarters Services, Directorate for Information Operations and Reports, 1215 Jefferson Davis Highway, Suite 1204, Arlington, VA 22202-4302, and to the Office of Management and Budget, Paperwork Reduction Project (0704-0188), Washington, DC 20503.

1. AGENCY USE ONLY (Leave blank)		2. REPORT DATE December 15, 1998	3. REPORT TYPE AND DATES COVERED Annual Report 1 Dec. 97 - 30 Nov. 98	
4. TITLE AND SUBTITLE Annual Report on Application of Model-Based Signal Processing Methods to CEM Simulators			5. FUNDING NUMBERS Research Grant ONR N00014-98-1-0178	
6. AUTHOR(S) Hao Ling				
7. PERFORMING ORGANIZATION NAMES(S) AND ADDRESS(ES) The University of Texas at Austin Department of Electrical and Computer Engineering Austin, TX 78712-1084			8. PERFORMING ORGANIZATION REPORT NUMBER No. 1	
9. SPONSORING / MONITORING AGENCY NAMES(S) AND ADDRESS(ES) Office of Naval Research Ballston Centre Tower One 800 North Quincy Street Arlington, VA 22217-5660 Program Officer Wen Masters ONR 311			10. SPONSORING / MONITORING AGENCY REPORT NUMBER	
11. SUPPLEMENTARY NOTES				
a. DISTRIBUTION / AVAILABILITY STATEMENT Approved for Public Release Distribution Unlimited			12. DISTRIBUTION CODE	
13. ABSTRACT (Maximum 200 words)  This report summarizes the scientific progress on the research grant "Application of Model-Based Signal Processing Methods to Computational Electromagnetics Simulators" during the period 1 December 1997 - 30 November 1998. Progress on model-based frequency extrapolation of antenna radiation patterns on complex platforms and extraction of sparse representation of antenna radiation and coupling data is described.				
14. SUBJECT TERMS Computational electromagnetics, model-based signal processing			15. NUMBER OF PAGES 65	
			16. PRICE CODE	
17. SECURITY CLASSIFICATION OF REPORT Unclassified	18. SECURITY CLASSIFICATION OF THIS PAGE Unclassified	19. SECURITY CLASSIFICATION OF ABSTRACT Unclassified	20. LIMITATION OF ABSTRACT	

**ANNUAL REPORT ON**

**APPLICATION OF MODEL-BASED SIGNAL  
PROCESSING METHODS TO COMPUTATIONAL  
ELECTROMAGNETICS SIMULATORS**

**Office of Naval Research  
Research Grant N00014-98-1-0178**

**For the period December 1, 1997 through November 30, 1998**

**Submitted by**

**Professor Hao Ling**

**Department of Electrical and Computer Engineering  
The University of Texas at Austin  
Austin, TX 78712-1084**

**December 15, 1998**

## **APPLICATION OF MODEL-BASED SIGNAL PROCESSING METHODS TO COMPUTATIONAL ELECTROMAGNETICS SIMULATORS**

Project Starting Date: Dec. 1, 1997

Reporting Period: Dec. 1, 1997 – Nov. 30, 1998

Principal Investigator: Professor Hao Ling  
(512) 471-1710  
ling@ece.utexas.edu

Graduate Students: T. Su, Y. Wang, C. Ozdemir

Research Associate: R. Bhalla (1 month)

**A. SCIENTIFIC OBJECTIVES:** The objective of this research program is to apply model-based signal processing methods to enhance the performance of computation electromagnetics (CEM) simulators for shipboard antenna design. While recent advances in CEM algorithms has significantly reduced the simulation cost of modeling complex radiation and scattering phenomena, real-world engineering design and optimization often require that calculations be carried out repeatedly over large parameter spaces such as frequency and aspect angle, making the computation cost still exceedingly high. The goal of this research is to apply model-based signal processing algorithms to CEM simulators to overcome such computational bottleneck and achieve higher design throughput. In particular, we shall address the issue of how to interpolate and extrapolate the frequency behaviors of antenna characteristics based on a sparse set of computed data. We shall also extend this methodology from the frequency to the spatial dimension to map out radiation field behaviors on a complex platform. Finally, we shall explore the transportability of the methodology to other applications such as radar signatures and wireless channel characteristics.

**B. SUMMARY OF RESULTS AND SIGNIFICANT ACCOMPLISHMENTS:** The focus during the first year of this research program is twofold. First, we set out to devise algorithms to extrapolate the frequency behavior of antenna radiation characteristics on



complex platforms from a limited set of computed data. Our approach is based on applying a time-of-arrival model to the induced current on the platform and using the superresolution algorithm ESPRIT to estimate the model parameters. Second, we set out to parameterize complex antenna radiation patterns using a sparse point radiator model. Our approach is based on a matching pursuit algorithm that extracts the relevant radiation physics contained in the signal. The main computational engine of focus is the code FISC, which employs the fast multipole technology. The detailed descriptions of these two areas are described below. They are followed by discussions on some exploratory efforts in other related topics.

**Model-based frequency extrapolation of antenna radiation patterns on complex platforms.** In antenna design and analysis, the mounting platform can have a significant effect on the antenna radiation characteristics. However, rigorous solution of the radiation problem over a complex platform is very time consuming, and the computation complexity increases dramatically as the frequency increases. During the past year, we have developed a model-based frequency extrapolation technique with which the radiated field over a broad band of frequencies can be obtained using rigorously computed results at low frequencies. Our approach entails three steps. First, the induced current on the platform surface is computed at low frequencies using a CEM solver. For this purpose, we have transported the fast multiple method (FMM) based code FISC, originally developed by the University of Illinois on the UNIX platform, to the Windows NT environment. We have demonstrated the capability of solving 3-D problems of up to 20 electrical wavelengths (over 30,000 unknowns) on a desktop PC. We have incorporated basic antenna modeling capabilities into FISC, which is originally developed for radar scattering applications. We have validated FISC results against measurements and other high-frequency codes on several canonical configurations. Lastly, we have demonstrated the capability to generate frequency-aspect antenna radiation data for 3-D ship-like platforms.

The extrapolation algorithm is based on applying the time-of-arrival model to the current on each basis element on the surface. In this model, we assume that the total

current is induced by different scattering mechanisms, as shown in Fig. 1. Each of the incident mechanism has a distinct arrival time, so that the current can be written as

$$J(\omega) = \sum_{n=1}^N a_n e^{-j\omega t_n} \quad (1)$$

where  $\omega$  is the angular frequency,  $N$  is the total number of incident mechanisms and  $t_n$  is the arrival time of the  $n^{\text{th}}$  incident mechanism. The model coefficients  $a_n$  and  $t_n$  are obtained using the superresolution algorithm ESPRIT [1], which is based on the model that the signal consists of a sum of exponential and additive white noise. Given a sequence with  $M$  samples, the algorithm can estimate the number of exponential  $N$  and determines the amplitude and period of each exponential term. The basic requirement in the number of samples is  $M > 2N + 1$ . Once the model parameters are found, the induced current at higher frequencies can be computed using (1). The radiated field is then obtained from the extrapolated current.

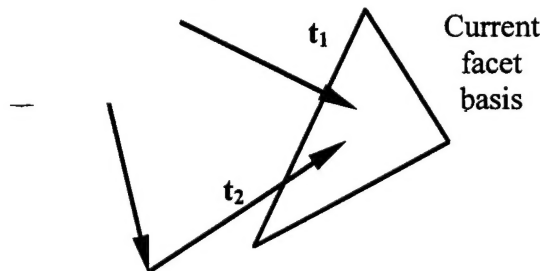


Fig. 1. Time-of-arrival model

As an example, we consider an antenna radiating in the presence of a 3-D structure shown in Fig. 2. The induced current is rigorously computed over the frequencies from 0.15 to 0.24 GHz at an interval of 0.01 GHz. The computation is done by FISC. The current is then extrapolated and the radiated field is computed. The extrapolation result is compared with the reference field data, which is also computed by FISC over the frequency band from 0.15 to 0.45 GHz at  $\theta = 50^\circ$  and  $\phi = 0^\circ$ , as shown in Fig. 3(a). The corresponding time domain response obtained via an inverse Fourier

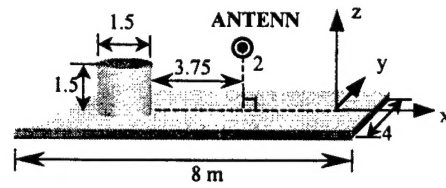
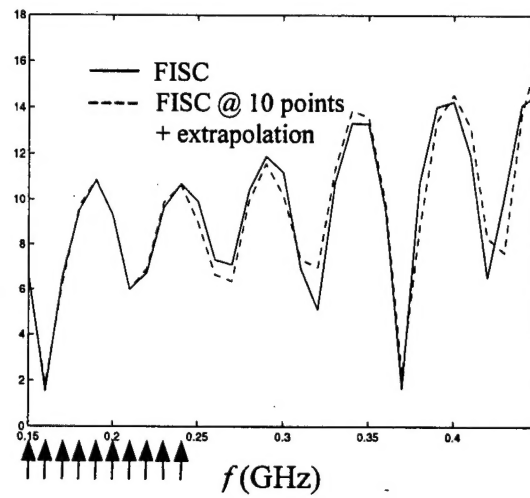
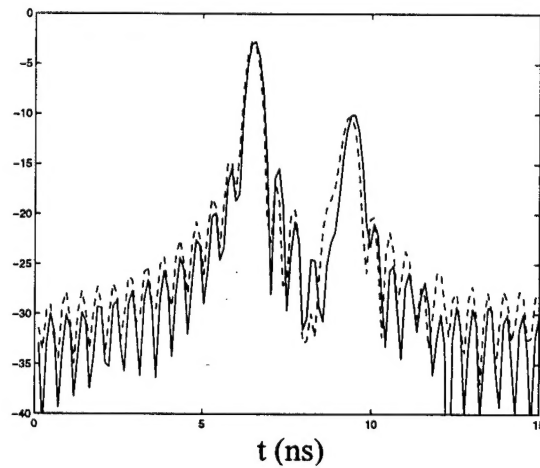


Fig. 2. Geometry of 3-D platform.



(a) Frequency domain response (dB)



(b) Time domain response (dB)

Fig. 3. Frequency Extrapolation

transform of the frequency data is plotted in Fig. 3 (b). We observe that the agreement between the two is good in both the frequency and time domains.

While the above approach is similar to that we had developed previously in [2] and [3] for radar signature extrapolation, several new challenges have been identified in the present antenna radiation problem. First, the scattering off the platform from antenna radiation is dominated by close-by interactions because of the  $1/r$  space loss. It is therefore more difficult to temporally resolve these closely spaced scattering mechanisms. This leads to a large bandwidth requirement in the CEM computation. Second, we found that the frequency dependence from the antenna is significant and must be incorporated into the model. In addition, the frequency dependence of different scattering components of each current element could be different, due to different scattering physics. Further incorporation of these effects should further enhance the accuracy of the extrapolation. Third, we suspect the results of FISC for near-field source problem may not be as accurate as that from the far field incidence. Work is ongoing to quantify and further overcome these limitations.

**Extraction of sparse representation of antenna radiation and coupling data.** Task 1 focuses on the utilization of model-based processing to extrapolate CEM data for the “forward” solution of antenna characteristics in the presence of complex platforms. An equally important problem from the design perspective is the “inverse” algorithm of spatially pinpointing the locations of platform scattering based on CEM data. Toward this end, we had previously developed a method to extract sparse model of the antenna radiation pattern on a complex platform [4],[5]. This representation is based on a point radiator model that describes the radiation pattern by a collection of “radiation centers” on the platform. The methodology for obtaining the radiation center model entails first generating the 3-D antenna synthetic aperture radar (ASAR) imagery of the platform, and then parameterizing the resulting image by a collection of point radiators via the CLEAN algorithm [6],[7]. Once such a representation is obtained, we can rapidly reconstruct antenna radiation patterns over frequencies and aspects with good fidelity. Thus such a model can be used for real-time reconstruction of complex antenna patterns in high-level system simulations. Furthermore, the resulting radiation center information can be used

to pinpoint cause-and-effect in platform scattering and provide important design guidelines for antenna placement and optimization. However, the method was based on a Fourier-based algorithm that relied on a number of small-angle, small-bandwidth approximations. Furthermore, the concept was only demonstrated using high-frequency ray-tracing simulations and not more rigorous CEM data.

During the past year, we have overcome the above deficiencies by developing a more generalized matching pursuit algorithm in the frequency-aspect domain based on a point radiator basis. We have also demonstrated the feasibility of extracting a sparse model of the antenna-platform interaction using CEM data from FISC. The matching pursuit algorithm is implemented based on the following radiation center basis:

$$E^s(k, \theta, \phi) = Ae^{-jkr_0} e^{jk(x_0 \sin \theta \cos \phi + y_0 \sin \theta \sin \phi + z_0 \cos \theta)} = Ae^{-jkr_0} e^{j(k_x x_0 + k_y y_0 + k_z z_0)} \quad (2)$$

where  $k$  is the wave number,  $(x_0, y_0, z_0)$  is the location of the radiation center. The origin of the above basis is illustrated in Fig. 4. Note that the phase factor in (2) accounts for the path delay from the antenna to the point scatterer on the platform, and then to the observation direction in the far field. To speed up the parameterization time of the matching pursuit algorithm, we estimate the location of the radiation centers by utilizing the Fourier-based ASAR algorithm. The point with the highest intensity is first located in the ASAR image and its amplitude and coordinates are determined to serve as an estimate of the strongest radiation center. We next zoom in on the precise location of the radiation center via a fine search. We then subtract the contribution of this radiation center from the total radiated field and iterate the process until the energy in the residual signal has reached a sufficiently small level.

As an example, the radiation center model is extracted from the computed radiation data from FISC for the structure shown in Fig. 2. The frequency range of the radiated field is from 0.6 to 0.9 GHz. The angular range of observation is over a 30-degree window in both azimuth and elevation. The first 10 extracted radiation centers are shown in Fig. 5, with their amplitudes represented by grayscale. We observe that the dominant platform scattering comes from the edge diffraction from the right edge of the platform and the corner structure formed by the cylinder and plate. Note that the

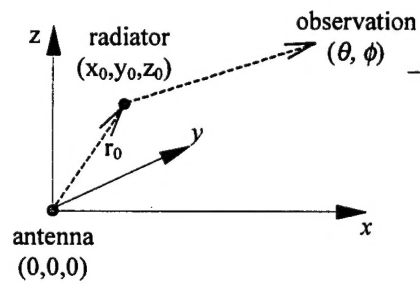


Fig. 4. Radiation center model

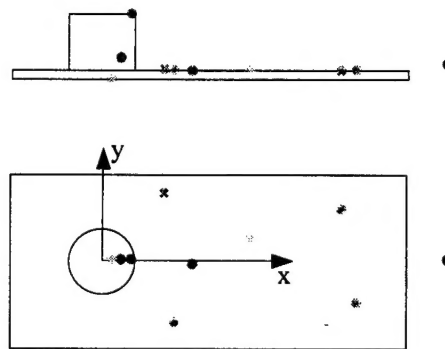


Fig. 5. Extracted radiation centers

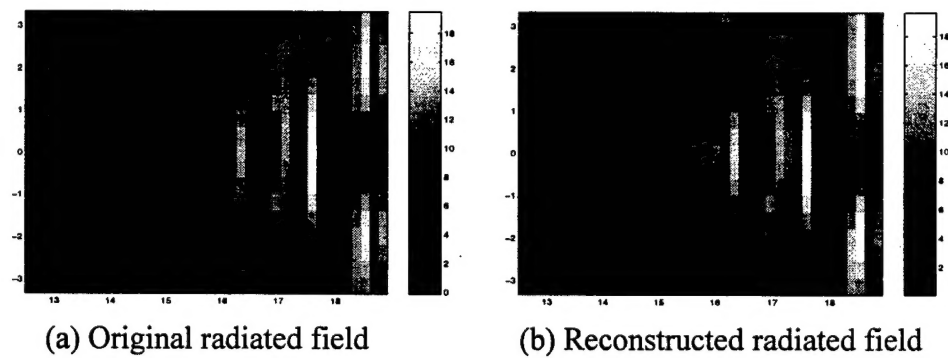


Fig. 6. Reconstruction of the radiated field from the radiation center model.

radiation center due to the edge diffraction is slightly off the platform. This is due to the limited resolution of the matching pursuit algorithm. Once the sparse representation is generated, the radiated field can be easily reconstructed using the radiation centers. The original radiated field at  $k_z = 0$  is plotted in Fig. 6(a) as a function of the  $k_x$  and  $k_y$ , where  $k_x$ ,  $k_y$  and  $k_z$  are defined in (2). The field reconstructed from the first 10 radiation centers is shown in Fig. 6(b). The two patterns match well over both frequency and angle. Thus the radiation pattern is efficiently approximated by the radiation center model.

We shall continue to refine this algorithm and examine more complex topside structures. In addition, in preparation for attacking the near-field antenna-to-antenna coupling problem, we have extended the ASAR concept to the near-field coupling scenario between antennas. This new algorithm is termed ACSAR (Antenna Coupling Synthetic Aperture Radar) [11]. We plan to utilize this model for addressing the antenna coupling issue once the CEM capability for simulating antenna coupling characteristics is in place.

**Other exploratory topics.** Several additional studies have been initiated during the past year and are described below. They serve as possible launching points into more relevant and focused efforts for the present program in the next year.

We have begun to investigate the resonant behaviors of antenna-platform configurations. This topic is motivated by the interest of the Navy SPAWAR Center in HF antennas where ship body resonances can dominate the antenna frequency characteristics. In the lower frequency regime, the scattering phenomenology differs from ray-optical characteristics. Consequently, the time-of-arrival model we have utilized successfully may no longer be efficient in this regime. We are carrying out a preliminary study to understand the scattering phenomenology in these configurations. Once we have a better grasp of the scattering physics, we plan to devise model-based parameterization strategies to efficiently compute antenna characteristics in the resonant region.

An important issue related to the study of resonant region using an iterative CEM solver like FISC is that when the platform exhibits strong resonance effect, the iteration number required for an accurate solution can become large. A good preconditioner for the moment matrix is needed to alleviate this problem. We have been investigating the

use of wavelet packet basis for the efficient sparsification of moment matrix under previous support from the Joint Services Electronics Program [8-10]. A possible extension of that research is that a good preconditioner could be found using such a wavelet representation. We plan to further investigate this topic with the resonant region calculation as a possible end-application.

Finally, we have begun to investigate the interpolation problem for CEM data. In contrast to our extrapolation work thus far, the interpolation problem is believed to be more stable in general. Although the potential payoff of an interpolation algorithm is not as great as extrapolation, it may provide a more robust way to achieve computational savings. One related study we have carried out recently is to construct radar images from unevenly undersampled data in the angular domain [13]. We have devised an algorithm that uses a matching pursuit engine in place of the Fourier transform in the image construction procedure. The algorithm entails searching and extracting out individual target scattering features one at a time in an iterative fashion. Therefore the strong interference between different target scattering features can be reduced. After all the main features are extracted, they can be displayed in the same image plane without the aliasing effect in the final radar image. The application of this work was aimed at constructing images from measured radar data. However, based the success we have had in this application, we believe the same approach may be applicable for interpolating CEM data which are sparsely populated on an unevenly sampled grid. We are currently pursuing this topic in more detail.

### **C. FOLLOW-UP STATEMENT:**

During the coming year, our research efforts will be devoted to two areas. In the first area, we will continue to refine the model-based algorithms we have developed for frequency extrapolation and sparse model extraction. The main objective will be to make the algorithms more stable and accurate. We also plan to study more complex platforms in order to investigate additional radiation physics and demonstrate the utility of the algorithms for more realistic configurations. In the second area, we will explore several new topics outlined in the last part of Section B. We will begin a more focused study of the antenna radiation characteristics in the resonant region. We also plan to initiate an



investigation into the antenna near-field coupling problem. It is anticipated that some efforts will be needed to upgrade the existing CEM capability to simulate the antenna characteristics for these different scenarios. Finally, we will extend our previous work on interpolating undersampled measured data to the present CEM acceleration application.

#### D. REFERENCES:

1. R. Roy, A. Paulraj and T. Kailath, "ESPRIT – a subspace rotation approach to estimation of parameters of cisoids in noise," *IEEE Trans. Acoust., Speech, Signal Processing*, vol. ASSP-34, pp. 1340-1342, October 1986.
2. Y. Wang, H. Ling, J. Song and W. C. Chew, "A frequency extrapolation algorithm for FISC," *IEEE Trans. Antennas Propagat.*, vol. 45, pp. 1891-1893, December 1997.
3. Y. Wang and H. Ling, "Radar signature prediction using moment method codes via a frequency extrapolation technique," submitted to *IEEE Trans. Antennas Propagat.*, February 1998.
4. C. Ozdemir, R. Bhalla, L. C. Trintinalia and H. Ling, "ASAR - antenna synthetic aperture radar imaging," accepted for publication in *IEEE Trans. Antennas Propagat.*, July 1998.
5. C. Ozdemir, R. Bhalla and H. Ling, "A radiation center representation of antenna radiation pattern on a complex platform," submitted for publication in *IEEE Trans. Antennas Propagat.*, September 1997.
6. R. Bhalla, J. Moore and H. Ling, "A global scattering center representation of complex targets using the shooting and bouncing ray technique," *IEEE Trans. Antennas Propagat.*, vol. AP-45, pp. 1850-1856, December 1997.
7. R. Bhalla, H. Ling, J. Moore, D. J. Andersh, S. W. Lee and J. Hughes, "3D scattering center representation of complex targets using the shooting and bouncing ray technique," *IEEE Antennas Propagat. Mag.*, vol. 40, pp. 30-39, October 1998.
8. H. Deng and H. Ling, "Fast solution of electromagnetic integral equations using adaptive wavelet packet transform," accepted for publication in *IEEE Trans. Antennas Propagat.*, July 1998.
9. H. Deng and H. Ling, "Efficient representation of moment matrix with pre-defined wavelet packet basis," *Elect. Lett.*, vol. 34, pp. 440-441, March 1998.

10. H. Deng and H. Ling, "On a class of pre-defined wavelet packet bases for efficient representation of electromagnetic integral equations," submitted for publication in *IEEE Trans. Antennas Propagat.*, October 1998.

## E. PUBLICATIONS:

### I. LIST OF JOURNAL ARTICLES (ONR supported in whole or in part)

11. C. Ozdemir and H. Ling, "ACSAR - antenna coupling synthetic aperture radar imaging algorithm," to appear in *J. Electromag. Waves Applications*, March 1999.
12. Y. Wang and H. Ling, "A model-based angular extrapolation technique for iterative method-of-moments solvers," to appear in *Microwave Optical Tech. Lett.*, February 1999.
13. Y. Wang and H. Ling, "Adaptive ISAR image construction from unevenly undersampled data," submitted for publication in *IEEE Trans. Antennas Propagat.*, November 1998.

### II. LIST OF CONFERENCE PROCEEDINGS (ONR supported in whole or in part)

14. C. Ozdemir, R. Bhalla and H. Ling, "Radiation center representation of antenna synthetic aperture radar (ASAR) images," International IEEE AP-S Symposium, pp. 338-341, Atlanta, GA, June 1998.
15. C. Ozdemir and H. Ling, "Synthetic aperture radar imaging algorithm for antenna coupling," International IEEE AP-S Symposium, pp. 342-345, Atlanta, GA, June 1998.
16. Y. Wang, H. Ling, J. Song and W. C. Chew, "Radar signature extrapolation for FISC," International IEEE AP-S Symposium, pp. 358-361, Atlanta, GA, June 1998.
17. T. Su and H. Ling, "Determining the equivalent impedance boundary condition for material-coated corrugated gratings based on the genetic algorithm," International IEEE AP-S Symposium, pp. 38-41, Atlanta, GA, June 1998.
18. T. Su, Y. Wang and H. Ling, "Model-based frequency extrapolation of antenna radiation characteristics on complex platforms," submitted for presentation at the 14th Annual Review of Progress in Applied Computational Electromagnetics, Monterey, CA, March 1999.
19. T. Su, Y. Wang and H. Ling, "Frequency extrapolation and model-based parameterization of antenna-platform radiation," submitted for presentation at the 1999 International IEEE AP-S Symposium, Orlando, FL, July 1999.

### III. LIST OF RELATED PRESENTATIONS

20. "Fast postprocessing algorithms for fast CEM solvers," AFOSR Electromagnetics Workshop, San Antonio, Texas, January 8, 1998.
21. "MSTAR Predict research at the University of Texas," DARPA MSTAR Program Predict Module Review, DEMACO, Champaign, Illinois, January 21, 1998.
22. "Fast postprocessing algorithms for fast CEM solvers," Industry-Government-CCEM Workshop on Computational Electromagnetics, Champaign, Illinois, April 3, 1998.
23. "Fast postprocessing algorithms for fast CEM solvers," 1998 Electromagnetics Code Consortium Annual Meeting, Army Research Laboratory, Adelphi, Maryland, May 5, 1998.
24. "Application of model-based techniques to computational electromagnetics simulators," Navy H-Infinity Program Kickoff Meeting, Navy SPAWAR System Center, San Diego, California, June 3, 1998.
25. "Electromagnetic signature simulation and feature extraction for radar target identification," Naval Research Laboratory, Radar Division Seminar, Washington DC, July 8, 1998.
26. "Signature exploitation research at UT-Austin," Mission Research Corporation, Dayton, OH, October 28, 1998.
27. "Modeling and simulation of scattering and radiation phenomena using scattering centers and radiation centers," Sensor Technologies Integration Laboratory, Air Force Wright Lab, Dayton, OH, October 29, 1998.

### IV. LIST OF THESES AND DISSERTATIONS

#### Ph.D.

C. Ozdemir, "Synthetic aperture radar algorithms for imaging antenna-platform scattering," August 1998.

### V. CONTRACTS AND GRANTS

H. Ling, "Time-frequency feature extraction from electromagnetic backscattered data," Joint Services Electronics Program, April 1, 1995 - March 31, 1998.

H. Ling, "Advanced studies of electromagnetic scattering," Wright-Patterson Air Force Base (via DEMACO, Inc.), June 1, 1995 - August 1, 1998.

W. Vogel, H. Ling and H. Foltz, "An automated cellular base-station siting tool for urban locations," Texas Advanced Technology Program, January 1, 1996 - August 31, 1998.

R. Chen and H. Ling, "Si CMOS process-compatible optical vias for intra- and inter- multi-chip-module optoelectronic interconnects," Texas Advanced Technology Program, January 1, 1996 - August 31, 1998.

H. Ling, "Advanced research and development for the MSTAR prediction module," Defense Advanced Research Project Agency (via DEMACO, Inc.), June 1, 1995 - December 31, 1998.

H. Ling, "MURI center for computational electromagnetics research," Air Force Office of Scientific Research (via Univ. of Illinois), December 15, 1995 - December 14, 2000.

H. Ling, "Application of model-based signal processing methods to computational electromagnetics simulators," Office of Naval Research, December 1, 1997 - November 30, 2000.

H. Ling, "Radar image enhancement, feature extraction and motion compensation using joint time-frequency techniques," Office of Naval Research, April 15, 1998 - April 14, 2001.

H. Ling, "Moving target modeling and simulation," Air Force Research Laboratory (via DEMACO, Inc.), October 1, 1998 - June 30, 2000.

H. Ling, "Electromagnetic scattering from periodic surfaces," Lockheed Martin Corporate Grant, November 15, 1998 - December 31, 1999.

#### **F. INTERACTIONS/COLLABORATIONS WITH NAVY SCIENTISTS:**

A kickoff meeting of the H-infinity program was held at the Navy SPAWAR Center in San Diego on June 3-4, 1998. One action item from the meeting is for us to interact with Dr. Dave Schwartz of SPAWAR on near-field data modeling. We plan to generate near-field data on test configurations and share them with Dr. Schwartz, who is interested in extending the H-infinity approach to antenna coupling data in the HF band. Through Drs. Jay Rockway and Peter Li of SPAWAR, we also became more aware of Navy's needs in the antenna design area, and have taken steps to adjust our research goals

to address issues more relevant to the Navy. Finally, we are planning to collaborate with Prof. Jianming Jin of the University of Illinois, who participated in the kickoff meeting as an ONR Young Investigator. Prof. Jin has developed a highly efficient finite-element solver for cavity scattering problems. He has recently provided a copy of the code to us for further testing and development. We plan to investigate the suitability of the code for modeling complex cavity structures embedded in ship platforms.

We have also been working closely with Dr. Victor Chen of Naval Research Lab on a separate Navy program in applying joint time-frequency processing to inverse synthetic aperture radar imagery. Some cross-fertilization of ideas with the H-infinity program can be expected since a good physical understanding of electromagnetic scattering and radiation phenomena is the basis of our work in both programs.

**G. NEW DISCOVERIES, INVENTIONS, OR PATENT DISCLOSURES:**

None.

**H. HONORS AND AWARDS:**

Dr. Ling has been elected to IEEE Fellow for 1999 for his "contribution to the development of radar signature prediction and feature extraction techniques."

## **APPENDIX**

### **Publications Supported by ONR Grant**

*Journal of Electromagnetic Waves and Applications, Vol. 13, 285-306, 1999*

## **ACSAR-ANTENNA COUPLING SYNTHETIC APERTURE RADAR IMAGING ALGORITHM**

C. Ozdemir and H. Ling

Department of Electrical and Computer Engineering  
The University of Texas at Austin  
Austin, TX 78712-1084

**Abstract**—A synthetic aperture radar imaging technique called ACSAR for antenna coupling scenarios is introduced. It is shown that an ACSAR image of a platform can be formed by inverse-Fourier transforming the multi-frequency, multi-spatial coupling data between two antennas. Furthermore, we present a fast ACSAR imaging algorithm that is specifically tailored to the shooting and bouncing ray (SBR) technique. The fast algorithm is shown to reduce the total simulation time by several orders of magnitude without significant loss of fidelity. Finally, a sparse representation of ACSAR imagery is introduced by extracting the point radiators in the image. By parameterizing the ACSAR image, it is possible to reconstruct the 3-D ACSAR image and the 3-D frequency-spatial data with a very sparse set of radiation centers.

### **1. INTRODUCTION**

The electromagnetic coupling between antennas on a complex platform is an important issue in antenna design. For an antenna designer, it is useful to identify the areas on the platform that cause strong coupling between the antennas. In this work, we set out to develop an imaging algorithm to pinpoint the dominant scattering locations on the platform that give rise to antenna interactions from the coupling data between antennas. Our approach to this problem is based on the Inverse Synthetic Aperture Radar (ISAR) concept. ISAR imaging is a standard technique to map the locations of dominant scattering off a target based on the multi-frequency, multi-aspect backscattered data [1,2]. We have extended this concept previously to the far-field antenna

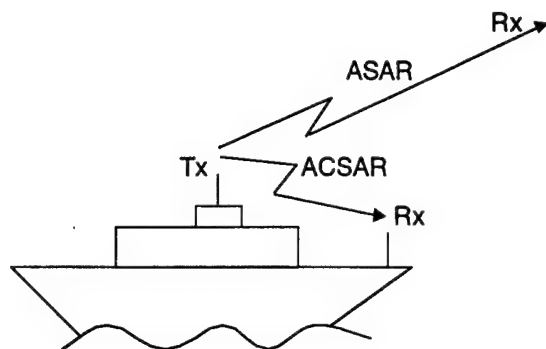


**Figure 1.** Comparison of the ASAR and the ACSAR scenario.

radiation problem by introducing the Antenna SAR (ASAR) imaging algorithm [3]. An ASAR image of a platform maps the strong secondary radiators on the platform from multi-frequency, multi-aspect radiation data in the far field. Such information can be useful to the antenna designer in mitigating platform effects. In this paper, we extend the ASAR concept to the near-field antenna coupling problem by generating the Antenna Coupling SAR (ACSAR) image of the platform (see Fig. 1). By collecting the multi-frequency, multi-spatial coupling data, it is shown that an ACSAR image of the platform can be formed to display the dominant scattering locations on the platform. To achieve the required spatial diversity, the data are collected on a 2-D grid at the receiver site.

This paper is organized as follows. First, we derive the ACSAR imaging algorithm. In Sec. 2, it is shown that under the single-bounce and small-bandwidth approximations, a Fourier transform relationship exists between the multi-frequency, multi-spatial coupling data and the 3-D locations of antenna-platform interaction. Hence, by 3-D inverse-Fourier transforming the coupling data, it is possible to image these scattering locations on the platform. This concept will be demonstrated by using the computed frequency-spatial data from the Shooting and Bouncing Ray (SBR) technique [4–6]. In section 3, we present a fast ACSAR imaging algorithm that is specifically tailored to the SBR technique. By taking advantage of the ray tracing information within the SBR engine, we demonstrate that a direct image-domain formation is possible without resorting to multi-frequency, multi-spatial calculations. The image-domain formation algorithm can be further acceler-



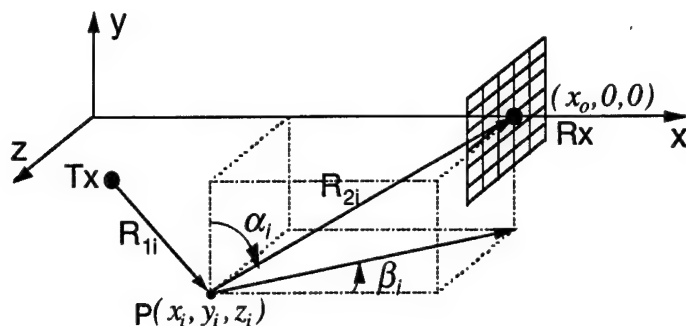


Figure 2. The geometry for ACSAR imaging.

ated by the application of the fast fourier transform (FFT) algorithm. The fast algorithm is compared to the general frequency-aperture algorithm in several numerical examples. It is also shown that the total computation time can be reduced from hundreds of hours to minutes without significant loss of fidelity. In Sec. 4, we further present a sparse model to represent ACSAR imagery. By parameterizing the ACSAR imagery with a set of point radiators on the platform, it is possible to reconstruct the 3-D ACSAR image and the 3-D frequency-spatial data with a very sparse set of radiation centers.

## 2. ACSAR IMAGING ALGORITHM

### 2.1 Formulation

We shall first derive the general ACSAR imaging algorithm that utilizes multi-frequency, multi-spatial radiation data in the near-field region of the platform. We assume the transmitter and receiver setup as depicted in Fig. 2. At the receiver site, spatial diversity on a two-dimensional aperture centered at  $(x_0, 0, 0)$  is used to achieve resolution in the two cross range dimensions. Similarly, to achieve down range resolution, frequency diversity is used. In addition to the direct radiation from the transmitter to the receiver, there are contributions from the antenna-platform interactions. The scattered electric field at the receiver site due to the scattering from a point  $P(x_i, y_i, z_i)$  on the platform can be written as

$$E_s(k) = A_i \cdot e^{-jkR_{1i}} \cdot e^{-jkR_2} \quad (1)$$

where  $A_i$  is the strength of the scattered field,  $R_{1i}$  is the path length from the transmitter antenna to  $P$ ,  $R_2$  is the path length from  $P$  to the receiver and  $k$  is the free-space wave number. Next, we will make two approximations to the above equation to arrive at a Fourier-based imaging algorithm. The first assumption, commonly used in ISAR imaging, is that the radiation data are collected within a certain frequency bandwidth that is small compared to the center frequency of operation. We will further assume that the size of the aperture at the receiver site is small compared to path length  $R_2$ . Combining these assumptions, we can approximate the phase lag in the second exponential term as follows:

$$kR_2 \cong kR_{2i} + k_0(y \cos \alpha_i + z \sin \alpha_i \sin \beta_i) \quad (2)$$

where  $\alpha_i$  and  $\beta_i$  are defined in Fig. 2,  $R_{2i}$  is the distance from  $P$  to the center of the 2-D aperture, and the variables  $y$  and  $z$  refer to spatial locations in the receiver aperture. The scattered electric field can thus be approximated by

$$E_s(k, y, z) = A_i \cdot e^{-jk(R_{1i} + R_{2i})} \cdot e^{-jk_0 y \cos \alpha_i} \cdot e^{-jk_0 z \sin \alpha_i \sin \beta_i} \quad (3)$$

In the above formula, a Fourier transform relationship exists between the variables  $(k, y, z)$  and  $(R_i = R_{1i} + R_{2i}, u_i = k_0 \cdot \cos \alpha_i, v_i = k_0 \cdot \sin \alpha_i \sin \beta_i)$ . By taking the 3-D inverse Fourier transform of the scattered field with respect to  $k$ ,  $y$ , and  $z$ , we obtain a 3-D ACSAR image of the platform as follows:

$$\begin{aligned} \text{ACSAR}(R, u, v) &= \text{IFT} \{E_s(k, y, z)\} \\ &= \text{IFT} \left\{ A_i \cdot e^{-jk \cdot R} \cdot e^{-jk_0 u} \cdot e^{-jk_0 v} \right\} \\ &= A_i \cdot \delta(R - R_i) \cdot \delta(u - u_i) \cdot \delta(v - v_i) \end{aligned} \quad (4)$$

Therefore, by inverse Fourier transforming the multi-frequency, multi-spatial coupling data, the point scatterer  $P$  will manifest itself as a peak in the image at  $(R_i, u_i, v_i)$  with amplitude  $A_i$ . In practice, since the frequency bandwidth and the aperture size are not infinite, the actual spot size of the point scatterer will be inversely proportional to the frequency bandwidth and the aperture size. Note that we have not

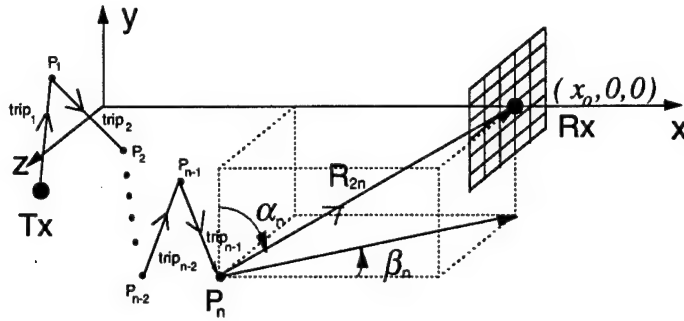


Figure 3. The geometry for a multiple bounce mechanism.

yet constructed the ACSAR image in the original  $(x, y, z)$  coordinates. However, it is straightforward to transform the ACSAR image from the  $(R, u, v)$  to the  $(x, y, z)$  coordinates by the following transformation formulas:

$$x = \frac{x_0^2 + R^2 - 2 \cdot R \cdot x_0 \cdot \sqrt{1+c}}{2 \cdot (x_0 - R \cdot \sqrt{1+c})} \quad (5a)$$

$$y = -\frac{(x_0 - x)}{\tan \alpha \cdot \tan \beta} \quad (5b)$$

$$z = \tan \beta \cdot (x_0 - x) \quad (5c)$$

$$c = \tan^2 \beta + \frac{1 + \tan^2 \beta}{\tan^2 \alpha} \quad (5d)$$

Since the transformation is not linear, it is not easy to estimate the distortion effect of the transformation on the ACSAR image. This issue will be addressed in the numerical examples as well in Sec 4.3. To summarize, the ACSAR imaging algorithm consists of three basic steps:

- (1) Collect multi-frequency, multi-spatial coupling data  $E_s(k, y, z)$ ,
- (2) Take the 3-D inverse Fourier transform of  $E_s(k, y, z)$  to form ACSAR( $R, u, v$ ),
- (3) Use (5) to generate ACSAR( $x, y, z$ ), the image in the platform coordinates.

In the resulting ACSAR image, the dominant scattering points on the platform due to platform interactions between the transmitter and the receiver will be manifested as peaks.

Several comments are in order. First, the present Fourier-based imaging algorithm is derived based on small bandwidth and small aperture approximations. Since these assumptions are similar to those made in the ISAR imaging algorithm, no attempts have been made by us in this paper to quantify the errors related to these approximations. Second, the present ACSAR algorithm is based on the single-bounce assumption. Therefore, multiple-bounce mechanisms will not be mapped correctly in the resulting ACSAR image. This situation is similar to the standard ISAR algorithm. We shall discuss how the multi-bounce mechanisms are manifested in the ACSAR image to guide us in image understanding. We consider an  $n$ -bounce scattering mechanism as shown in Fig. 3. The corresponding scattered electric field for this mechanism is given by

$$E_s(k, y, z) = A \cdot e^{-jk(\text{trip}_{\text{total}} + R_{2n})} \cdot e^{-jk_0 y \cos \alpha_n} \cdot e^{-jk_0 z \sin \alpha_n \sin \beta_n} \quad (6)$$

where  $\text{trip}_{\text{total}} = \text{trip}_1 + \dots + \text{trip}_{n-1}$  corresponds to the path that the wave travels from the transmitter to the last hit point and  $R_{2n}$  is the path length from the last hit point to the center of the aperture at the receiver site. By taking the 3-D inverse-Fourier transform of the above equation, we obtain a peak in the ACSAR image at  $(R_u, u_n, v_n)$  where  $R_n = \text{trip}_{\text{total}} + R_{2n}$ ,  $u_n = k_0 \cdot \cos \alpha_n$  and  $v_n = k_0 \cdot \sin \alpha_n \cdot \sin \beta_n$ . We observe that this corresponds nearly to the last hit point on the platform. The  $u$  and  $v$  values (and the corresponding  $\alpha$  and  $\beta$  angles) correspond exactly to those of the last hit points, while the  $R$  value corresponds to the cumulative delay of the mechanism. This means that a multiple-bounce mechanism will be mapped in the ACSAR image as a point shifted from the last hit point on the platform in a direction opposite to  $\hat{R}_{2n}$ , the vector from the last hit point to the receiver. This effect will be seen in the example next. Finally, in the ACSAR algorithm derivation only the scattered field is considered. If the total field is applied to the algorithm, the direct radiation from the transmitter to the receiver will be imaged at the transmitter location. Since this peak will likely be the strongest one in the image, it may pose a dynamic range problem as the other scattering mechanisms due to antenna-platform interactions may be overshadowed. For simulation data, the isolation of the scattered field contribution from the direct antenna radiation is straightforward. For measurement data, a separate calibration run to measure the direct antenna radiation may be required to remove its contribution from the total field.

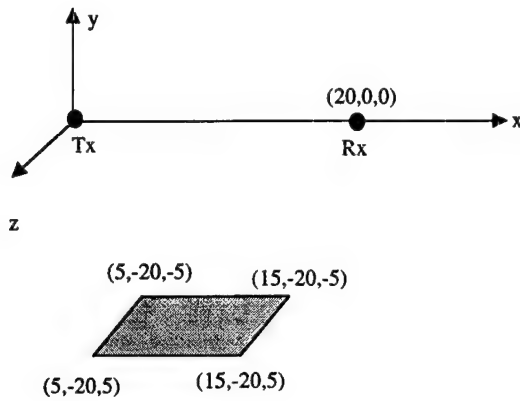


Figure 4. The geometry of the plate test example.

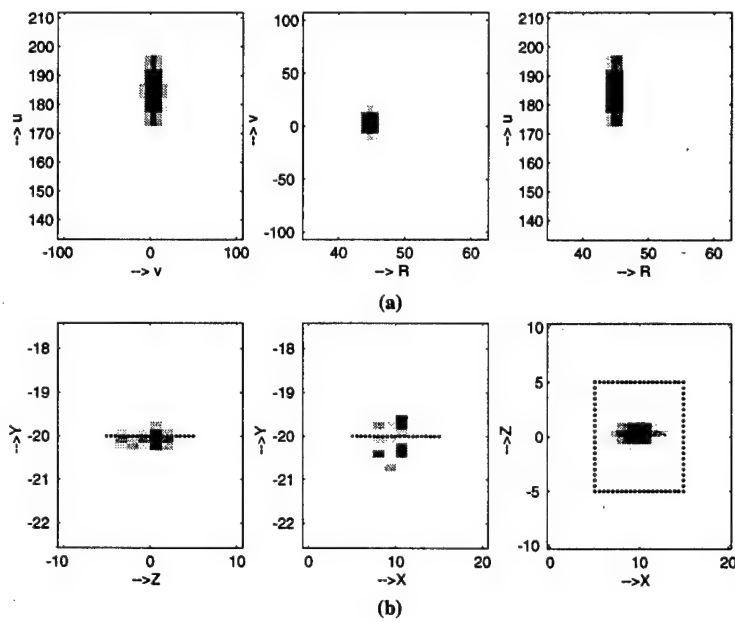


Figure 5. 2-D projected ACSAR images for the plate.

(a) In  $(R, u, v)$  coordinates.

(b) In  $(x, y, z)$  coordinates.

## 2.2 Numerical Example

The algorithm presented above is first tested using a simple configuration shown in Fig. 4. The platform is a perfectly conducting square plate of size 10m by 10m. The transmitter antenna is a half-wave dipole (at 10 GHz) and is located 20m above the plate. A total of 32 frequencies are computed within a 0.35 GHz bandwidth at the center frequency of 10 GHz. The simulation is carried out by a modified version of the SBR code Apatch [6]. The scattered field is collected on an aperture centered at (20m, 0, 0). The collection aperture consists of  $16 \times 32 = 512$  points, which range from -0.66m to 0.56m in 16 steps along the  $y$  direction and from -0.46m to 0.44m in 32 steps along the  $z$  direction. In the computed data only the scattered field from the platform is considered and the primary radiation due to the antenna is not included. Using the ACSAR algorithm, we first generate the 3-D ACSAR images in  $(R, u, v)$  domain. While applying the algorithm, a 3-D Hanning window is used prior to the FFT operation to suppress the sidelobes in the image. For display purpose, the 3-D ACSAR image is projected onto the 2-D  $R-u$ ,  $R-v$  and  $u-v$  plane as shown in Fig. 5(a). To view the ACSAR image in the platform  $(x, y, z)$  coordinates, we perform the necessary transformations in (5). The resulting 3-D ACSAR image is then projected onto the 2-D  $y-z$ ,  $x-y$ , and  $x-z$  planes as shown in Fig. 5(b). The dynamic range of the images is chosen to be 35 dB. According to the geometry, we expect a peak in the  $(x, y, z)$  image at (10m, -20m, 0) corresponding to the specular point on the plate. The corresponding  $R$ ,  $u$  and  $v$  values for this point are (44.72m, 186.4, 0). We observe from Figs. 5(a) and 5(b) that the peak occurs at the expected location. However, we notice that the specular peak is not as well focused in the  $xyz$ -plane as the  $Ruv$ -plane. This degradation is due to the additional  $(R, u, v)$ -to- $(x, y, z)$  transformation.

As the second example, we used a much more complex test platform called 'Slicy', whose CAD geometry is shown in Fig. 6. Slicy contains a number shapes on top of the platform including a closed cylinder, an open cylinder, a corner reflector and a step region. The platform is assumed to be perfectly conducting. A half-wave dipole is used as the transmitter and is placed at the origin. A total of 32 frequencies are computed within a 0.19 GHz bandwidth at the center frequency of 10 GHz. The scattered field is collected on an aperture centered

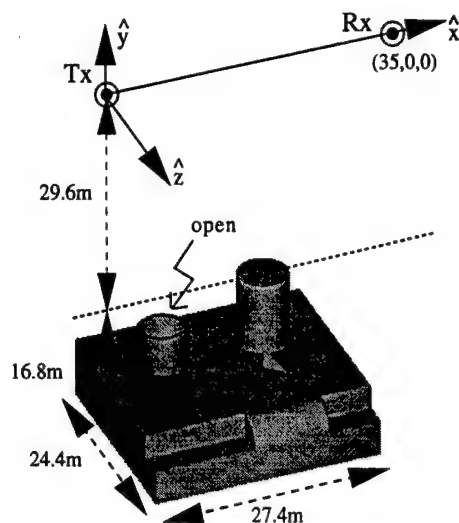
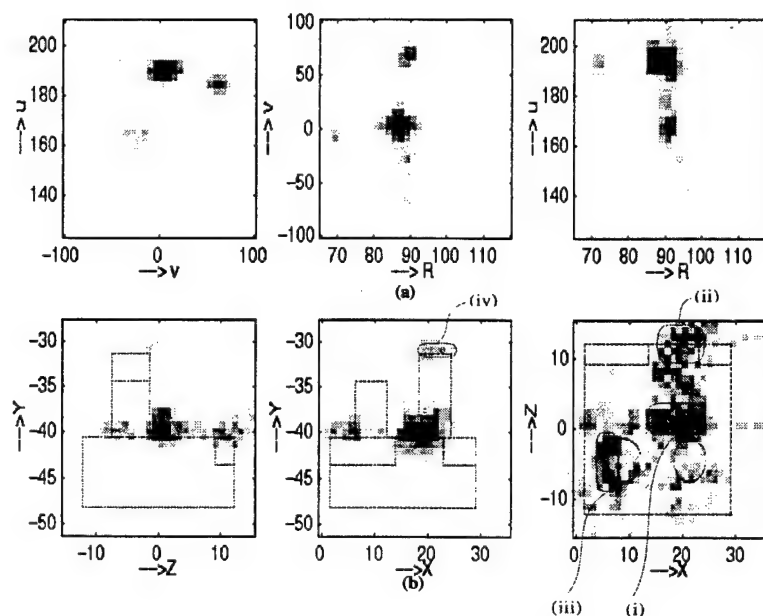


Figure 6. The geometry of the test example Slicy.

at (35m, 0, 0). There are  $32 \times 32 = 1024$  spatial points on the aperture, ranging from  $-1.14$  m to  $1.14$  m along the  $y$  direction and from  $-0.49$  m to  $0.49$  m along the  $z$  direction. The total computation time for the SBR simulation is about 160 hours on an IBM RS6000/590 workstation. Using the ACSAR algorithm, we generate the 3-D ACSAR image for the configuration. Again, a 3-D Hanning window is used to suppress sidelobes. The 3-D ACSAR image projected onto the 2-D  $R$ - $u$ ,  $R$ - $v$  and  $u$ - $v$  planes are shown in Fig. 7(a). Fig. 7(b) shows the projected ACSAR image in the platform  $(x, y, z)$  coordinates along the  $y$ - $z$ ,  $x$ - $y$  and  $x$ - $z$  planes. Also plotted in the images is the platform overlay. The dynamic range of the images is 35dB. We observe that the dominant scattering is from the middle of the platform around the point (17.5m,  $-40$ m, 0). This is the expected specular point on the platform (labeled as mechanism (i)). Also apparent is the scattering off the curved region between two steps (mechanism (ii)). This mechanism appears to be quite diffused in the image. We believe this is due to the distortion effect from the transformation in (5). A technique to alleviate this effect will be discussed in Sec. 4.3. We also observe some scattering mechanisms from the open cylinder (mechanism (iii)). Since the open cylinder is expected to create multiple bounces, the contribution in the image is shifted in the direction away from the re-



**Figure 7.** 2-D projected ACSAR images for Slicy

(a) In  $(R, u, v)$  coordinates.

(b) In  $(x, y, z)$  coordinates.

ceiver as discussed in the last section. As a result, it is located around the outside region of the open cylinder. Finally, the scattering off the top of the closed cylinder is labeled as mechanism (iv), although it is rather weak.

### 3. FAST ACSAR IMAGE GENERATION USING SBR

The ACSAR image formation algorithm discussed in the last section can be applied to either measurement or simulation data. In this section, we shall derive a fast ACSAR imaging algorithm specially tailored to the SBR technique. This is accomplished by utilizing the ray information within the SBR ray-tracing engine to generate the ACSAR image without resorting to any multi-frequency, multi-spatial calculations. We first derive an image-domain formula of ACSAR imaging [7]. Next, we implement a fast ray summation scheme [8,9] based on the image-domain formulation to reduce the total computation time. It is



demonstrated that an ACSAR image can be simulated at a fraction of the time as the brute-force frequency-aperture approach.

### 3.1 Image-Domain Formulation of ACSAR Imaging

In applying the SBR technique to the antenna-platform interaction problem, rays are first shot from the phase center of the transmitter and traced according to geometrical optics. At the exit point of each ray before they leave the platform altogether, a ray-tube integration is carried out to find the contribution of each ray to the field at the receiver. Under this construct, the scattered near field can be written as:

$$E_s(k, \phi, \theta) = \sum_{i \text{ rays}} \frac{jk}{2\pi} \cdot C_i \cdot (\Delta A)_{\text{exit}} S(\phi, \theta) \cdot e^{-jk \cdot \mathbf{r}_A} \quad (7)$$

where  $\mathbf{r}_A$  is the position vector from the last hit point  $A$  to the receiver,  $(\Delta A)_{\text{exit}}$  is the cross section of the exit ray tube,  $S(\phi, \theta)$  is the normalized radiation pattern from the ray tube and  $C_i$  is the field at the exit ray tube. For sufficiently small ray tubes,  $S(\phi, \theta)$  can be assumed to be unity. In the image-domain formulation, we will assume that the frequency bandwidth is small compared to the center frequency and the aperture size at the receiver site is small compared to the path length from the last hit point to the receiver. With these assumptions, we have  $\mathbf{k} \cdot \mathbf{r}_A \cong k \cdot R_2 + k_0 \cos \alpha \cdot y + k_0 \sin \alpha \sin \beta \cdot z$ . We further assume that the platform is perfectly conducting. (For non-perfectly conducting platforms, this derivation still applies as long as the frequency bandwidth is small.) Using these assumptions, we can let

$$\frac{jk}{2\pi} \cdot C_i \cdot (\Delta A)_{\text{exit}} \approx \sigma_i \cdot e^{-jk \cdot (\text{trip})_i} \quad (8)$$

where  $\sigma_i$  is assumed to be independent of frequency and  $(\text{trip})_i$  is the total path that the  $i$ 'th ray traveled from the transmitter to the last hit point. Consequently, the scattered electric field at the receiver can be written as

$$E_s(k, y, z) = \sum_{i \text{ rays}} \sigma_i \cdot e^{-jk(\text{trip}_i + R_{2i})} \cdot e^{-jk_0 \cos \alpha_i \cdot y} \cdot e^{-jk_0 \sin \alpha_i \sin \beta_i \cdot z} \quad (9a)$$

or by the change of variables similar to that in Sec. 2, we have simply

$$E_s(k, y, z) = \sum_{i \text{ rays}} \sigma_i \cdot e^{-jkR_i} \cdot e^{-ju_i \cdot y} \cdot e^{-jv_i \cdot z} \quad (9b)$$

Substituting the above equation to our ACSAR imaging formula, we get

$$\begin{aligned} \text{ACSAR}(R, u, v) &= \text{IFT}_3\{E_s(k, y, z)\} \\ &= \sum_{i \text{ rays}} \sigma_i \cdot \text{IFT}\{e^{-jkR_i}\} \cdot \text{IFT}\{e^{-ju_i \cdot y}\} \cdot \text{IFT}\{e^{-jv_i \cdot z}\} \end{aligned} \quad (10)$$

The inverse-Fourier transform operations in (10) can be performed in closed form with the result

$$\begin{aligned} \text{ACSAR}(R, u, v) &= \sum_{i \text{ rays}} \sigma_i \cdot \{2\Delta k \cdot e^{jk_0(R-R_i)} \text{sinc}(\Delta k(R-R_i))\} \\ &\quad \cdot \{2k_0\Delta y \cdot \text{sinc}(\Delta y(u-u_i))\} \\ &\quad \cdot \{2k_0\Delta z \cdot \text{sinc}(\Delta z(v-v_i))\} \end{aligned} \quad (11)$$

where  $\Delta k$  is the half bandwidth in frequency,  $\Delta y$  and  $\Delta z$  are the half-lengths of the aperture in  $y$  and  $z$ , respectively. We observe that the image-domain formulation gives the contribution of each ray to the total ACSAR image explicitly. Since  $\sigma_i$ ,  $(x_i, y_i, z_i)$  are available from the ray tracing, it is straightforward to calculate the corresponding  $(R_i, u_i, v_i)$  values. Therefore, given  $(\sigma_i, x_i, y_i, z_i)$  for each ray, we can form the ACSAR image directly by summing up the weighted 3-D sinc functions in (11).

### 3.2 Fast Algorithm

The image-domain expression of (11) is time consuming to carry out. We next apply a fast ray summation scheme to speed up the calculation in (11). We rewrite the image domain formula as

$$\text{ACSAR}(R, u, v) = \sum_{i \text{ rays}} \rho_i \cdot h(R-R_i, u-u_i, v-v_i) \quad (12a)$$

where  $\rho_i = 8 \cdot \sigma_i \cdot k_0^2 \Delta k \cdot \Delta y \cdot \Delta z$  and  $h(R, u, v)$  is the 3-D ray-spread function given by

$$h(R, u, v) = e^{jk_0 R} \text{sinc}(\Delta k \cdot R) \cdot \text{sinc}(\Delta y \cdot u) \cdot \text{sinc}(\Delta z \cdot v) \quad (12b)$$

We can cast (12a) as a convolution between a 3-D weighted impulse function and  $h$  as shown below:

$$\begin{aligned} \text{ACSAR}(R, u, v) &= \left\{ \sum_{i \text{ rays}} \rho_i \cdot \delta(R - R_i, u - u_i, v - v_i) \right\} * h(R, u, v) \\ &= g * h \end{aligned} \quad (13)$$

To speed up the computation time of the convolution, we use an FFT-based fast scheme proposed by Sullivan [9]. Since the 3-D weighted impulse train  $g$  is not uniformly spaced, we first interpolate the function onto a uniformly sampled grid. To ensure the accuracy of computation, we oversample the grid at  $N$  times the Nyquist rate. For the interpolation, we use a linear approximation to update the closest eight neighbors depending on their distances from the location of the original impulse. The detail of this scheme can be found in [3] and will not be repeated here. After applying the interpolation scheme, the ACSAR image can be generated by

$$\text{ACSAR}(R, u, v) = \text{IFFT}_3(\text{FFT}_3(g_s(R, u, v)) \cdot \text{FFT}_3(h(R, u, v))) \quad (14)$$

where  $\text{FFT}_3$  and  $\text{IFFT}_3$  are the three-dimensional forward and inverse fast Fourier transforms, respectively. The final  $\text{ACSAR}(x, y, z)$  image can be generated using the transformations in (5).

### 3.3 Numerical Example

The fast approach presented above is applied to the same Slicy geometry that was used in the frequency-aperture approach. In the interpolation grid, an over sampling ratio of  $N = 4$  is used in all three dimensions to ensure the accuracy of the computation. The results are depicted in Figs. 8(a) and 8(b) as 2-D projected ACSAR images in the three principal planes. Fig. 8(a) shows the images in the  $(R, u, v)$  coordinates, while Fig. 8(b) shows the images in the  $(x, y, z)$  coordinates. Again, a 3-D Hanning window is applied and the dynamic range of the images is chosen to be 35dB. By comparing these images with the images that are generated by using the frequency-aperture approach (Figs. 7(a) and 7(b)), we observe a fairly good agreement where all the key features are correctly simulated. The rms error between the frequency-aspect result and the image-domain result in the  $(R, u, v)$

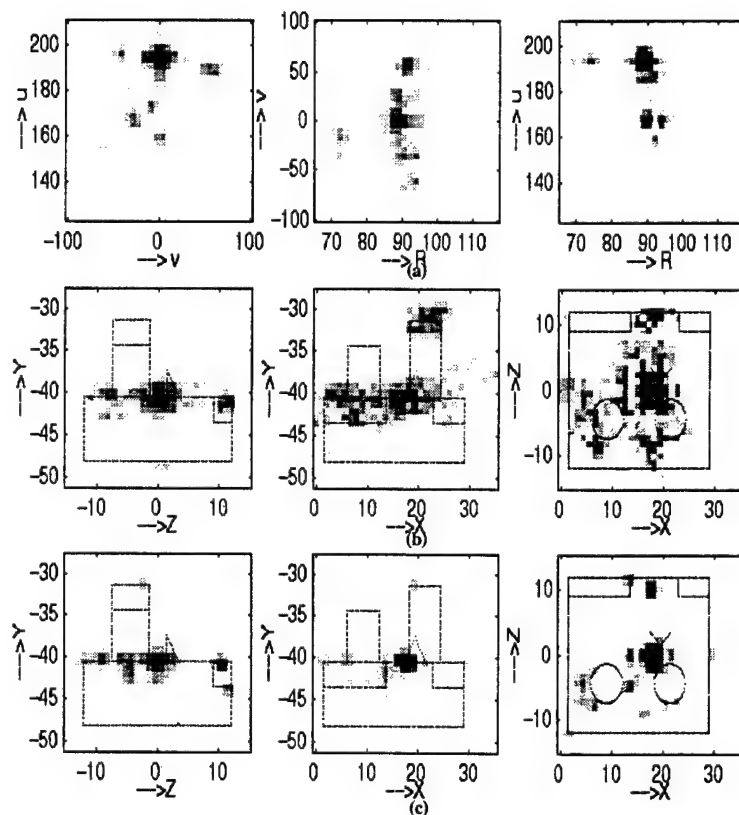


**Figure 8.** 2-D projected ACSAR images for Slicy using the fast algorithm.

- (a) Image formed in  $(R, u, v)$  coordinates.
- (b) Image transformed to  $(x, y, z)$  coordinates.
- (c) Image formed directly in  $(x, y, z)$  coordinates.

domain is calculated to be 2.13%. The image-domain results lead to a more focused image due to its small bandwidth approximation. This is consistent with our past experience from ISAR and ASAR algorithms. To show the time savings that we gain by using the image-domain approach, the total computation times of the frequency-aperture algorithm and the fast algorithm are compared in Table 1. The timings are divided into the ray-tracing time and the ray-summation time. As it can be seen from the table, the ray-tracing time of 9 minutes is the

**Table 1.** ACSAR simulation time for Slicy on an IBM RS6000/590 workstation.

	Ray Tracing Time	Ray Summation Time	Total Time
Frequency- Aperture Approach	9 minutes	161 hours	161 hours
Fast Algorithm	9 minutes	6 minutes	15 minutes

same for both approaches. Ray summation takes over 160 hours for the frequency-aperture approach and is the dominant portion of the total simulation time. The fast approach reduces the ray summation time to only 6 minutes.

In addition to large savings in simulation time, it is also possible to circumvent the image distortion effect due to the coordinate transformation by using the image-domain formulation. This is accomplished by generating the ACSAR image directly in the platform  $(x, y, z)$  coordinates in (12) instead of the  $(R, u, v)$  coordinates. To find the correct  $(x_i, y_i, z_i)$  position for a multi-bounce ray, we move along the direction opposite to the vector from the last hit point to the receiver. The amount of the shift is given by the cumulative trip of the ray. This has been discussed earlier in the image interpretation context in Sec. 2.1. In this manner, the image in the platform coordinate is updated one ray at a time using the 3-D ray-spread function in the  $(x, y, z)$  coordinate system, thereby eliminating the need to perform the transformation in (5). Fig. 8(c) shows the result of generating the image directly in the  $(x, y, z)$  coordinates. We observe that all the features are now much more focused than those in Fig. 8(b).

To summarize, we have demonstrated the feasibility to simulate ACSAR imagery using the SBR technique very rapidly. This is achieved by a combination of the image-domain formulation and an FFT-based fast algorithm. Furthermore, we have shown that it is possible to form the image in the platform coordinates directly by using this approach. This eliminates the need to perform the required coordinate transformation which can defocus the features in the image.

## 4. A SPARSE REPRESENTATION OF ACSAR IMAGERY

### 4.1 Point Radiator Model of ACSAR Imagery

In simulating the ACSAR image of the platform using SBR, tens of thousands of rays are shot onto the platform. Yet, as we can see from the resulting data, the ACSAR images are in fact quite sparse. This is because the rays interfere with each other to give rise to strong coherent scattering over a small, localized area on the platform. Hence, it may be possible to accurately represent the ACSAR image by a finite set of point "radiation centers" on the platform. This concept is similar to the scattering center representation in radar scattering problems [10,11]. We shall adopt a point radiator model which has the same form of (12a) to parameterize the ACSAR image

$$\text{ACSAR}(x, y, z) = \sum_{\substack{n \text{ radiation} \\ \text{centers}}} A_n \cdot h(x - x_n, y - y_n, z - z_n) \quad (15)$$

where  $h(x, y, z)$  is given in (12b) and  $A_n$  is the strength of the point radiator located at  $(x_n, y_n, z_n)$ . The remaining problem is to determine  $(A_n, x_n, y_n, z_n)$  to find a radiation representation for the image.

### 4.2 Extraction Using CLEAN

To perform the extraction process in (15), we apply the image processing algorithm CLEAN. CLEAN is a well-known extraction algorithm first developed in radio astronomy [12], and has been successfully applied for scattering center extraction [10]. It is a robust technique that successively picks out the highest point in the image and removes its point-spread function (assumed to be the ray-spread function in our case) from the image. At the  $n$ th iteration of CLEAN, if the strength of the point scatterer is  $A_n$ , the 3-D residual image can be written as

$$\begin{aligned} [3 - \text{D Residual Image}]_{n+1} = & [3 - \text{D Residual Image}]_n \\ & - [A_n \cdot h(x - x_n, y - y_n, z - z_n)] \end{aligned} \quad (16)$$

The above iteration process continues until the highest point in the residual image falls below to a user-defined threshold. Once we extract

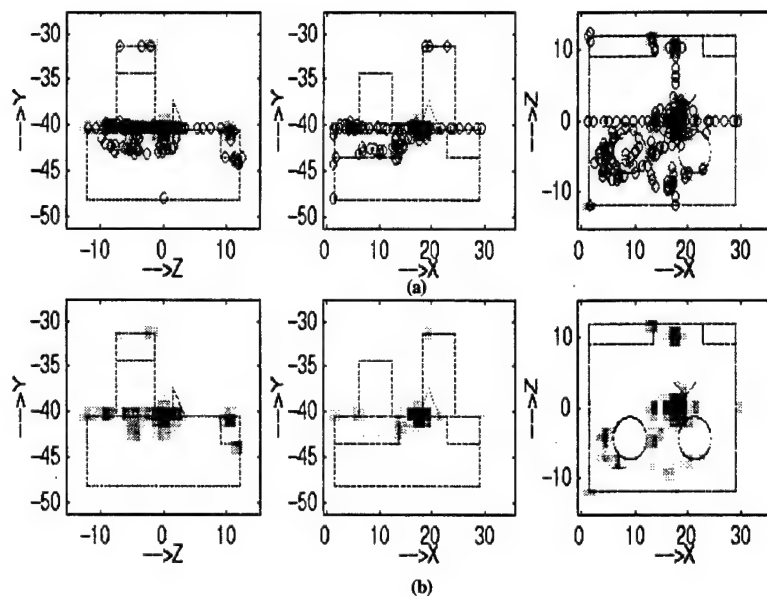


**Figure 9.** (a) The locations of the 150 extracted radiation centers. (b) 2-D projected ACSAR images reconstructed by using the extracted radiation centers.

the radiation centers from the image, we can reconstruct the multi-frequency and multi-spatial data by the formula:

$$E_s(k, y, z) = \sum_{n \text{ radiation centers}} A_n \cdot e^{-jk \cdot R_n} \cdot e^{-ju_n \cdot y} \cdot e^{-jv_n \cdot z} \quad (17)$$

where  $(R_n, u_n, v_n)$  are related to  $(x_n, y_n, z_n)$  through the transformation described earlier.

We apply the CLEAN extraction algorithm to the 'Slicy' example. We extract a total of 150 point radiators from the 3-D ACSAR image shown in Fig. 8(c). The locations of the extracted radiation centers are projected on three different 2-D planes and are shown as small circles in Fig. 9(a). As it can be seen from the figures, most of the radiation centers are located on the platform at  $y = -40\text{m}$ . The remainders are located on the top of tall cylinder and around the step region. We then reconstruct the ACSAR image using the radiation centers and they are shown in Fig. 9(b). We use the same dynamic range of 35dB when

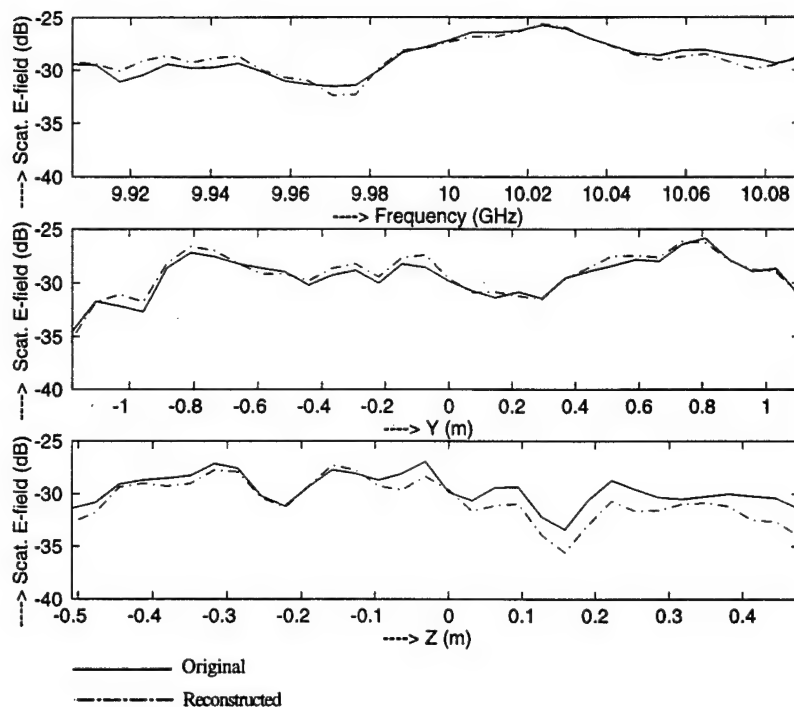


**Figure 10.** Comparison of the original and the reconstructed field patterns.

- (a) Frequency sweep at  $(35, 0, 0)$ .
- (b) Spatial comparison at 10 GHz along  $(35, y, 0)$ .
- (c) Spatial comparison at 10 GHz along  $(35, 0, z)$ .

plotting the images. By comparing the reconstructed ACSAR images to the reference image in Fig. 8(c), we see that the reconstruction is good. The rms error between the original and the reconstructed ACSAR images is calculated to be less than 0.1%. Next, we reconstruct the frequency and the spatial data by using the formula in (17). The original (solid) and the reconstructed (dashed) patterns are shown in Fig. 10. In Fig. 10(a), the frequency sweep comparison is made at the center point of the receiver. In Fig. 10(b) and 10(c), the spatial variation comparisons are made at the 10 GHz center frequency along the  $y$ -axis and along the  $z$ -axis, respectively. We observe a fairly good agreement for the frequency-spatial reconstruction by using the



radiation center model. Therefore, we can represent complex coupling data between antennas on a platform by using only a small set of point radiators. Such sparse data representation may be useful for data compression and system simulation applications.

#### 4.3. Eliminating Coordinate Transform Distortion Using CLEAN

We now describe a method that takes advantage of the CLEAN algorithm to eliminate the image distortion resulting from the  $(R, u, v)$ -to- $(x, y, z)$  coordinate transformation in the frequency-aperture image formation algorithm described in Sec. 2. In Sec. 3.3, we have already shown that this can be accomplished by using the image-domain formulation. However, the approach is only applicable when coupled to the SBR simulation. When data from measurement or other types of computational electromagnetics simulators are used, we must adopt a different strategy. Our approach is to first parameterize the image in the  $(R, u, v)$  coordinate system using the CLEAN algorithm. Once the image is parameterized by radiation centers located at  $(R_n, u_n, v_n)$ , we use (5) to find the corresponding  $(x_n, y_n, z_n)$  location of each radiation center in the platform coordinate. Then, the construction of the image in the platform coordinate is carried out using (15). Note that the main advantage of this approach is that the point-spread response in the final platform image is well-controlled. Consequently, the distorted point-spread response in the  $(x, y, z)$  coordinates is avoided in the platform image.

As an example, we apply this methodology to the ACSAR image in Fig. 7(a) by extracting a total of 150 radiation centers. After transforming these radiation centers into the platform coordinates, we form the ACSAR image directly in the  $(x, y, z)$  coordinates. The result is shown in Fig. 11. By comparing the new images to the images in Fig. 7(b), we observe that the mechanisms are much better focused using this approach. It is therefore the preferred step to generate the final platform image using the general frequency-aperture algorithm.

### 5. CONCLUSION

The ACSAR (antenna coupling synthetic aperture radar) imaging algorithm has been introduced to map platform scattering locations in

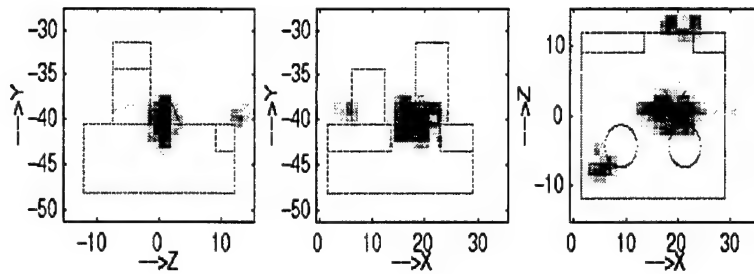


**Figure 11.** 2-D projected ACSAR images based on frequency-aperture data, formed by first parameterizing the  $(R, u, v)$  image using CLEAN and reconstructing the image in the  $(x, y, z)$  platform coordinates.

antenna coupling scenarios. It is shown that under the single-bounce and small-bandwidth approximations, a Fourier transform relationship exists between the multi-frequency, multi-spatial coupling data and the 3-D locations of antenna-platform interaction. Hence, by 3-D inverse-Fourier transforming the coupling data, it is possible to image the scattering locations on the platform. This concept has been demonstrated by using the computed frequency-spatial data from the SBR technique. However, the algorithm is general and can be applied to other simulation data or even measurements. Furthermore, we have presented a fast ACSAR imaging algorithm that is specifically tailored to the SBR technique. By taking advantage of the ray tracing information within the SBR engine, we have demonstrated that a direct image-domain formation is possible without resorting to multi-frequency, multi-spatial calculations. The image-domain formation algorithm can be further accelerated by the application of the FFT algorithm. The fast algorithm has been shown to reduce the total simulation time from hundreds of hours to minutes without significant loss of fidelity. Finally, we have presented a method to extract a sparse point-radiator model to represent ACSAR imagery. This is accomplished by parameterizing the ACSAR image with a set of point radiators on the platform using the CLEAN algorithm. Once such a sparse set of radiation centers have been extracted, it is possible to reconstruct the 3-D ACSAR image and the 3-D frequency-spatial data very rapidly with good fidelity.

## ACKNOWLEDGMENT

This work is supported by the Office of Naval Research under Contract No. N00014-98-1-0178 and in part by the Air Force MURI Center for Computational Electromagnetics under Contract No. AFOSR F49620-96-1-0025.

## REFERENCES

1. Mensa, D. L., *High Resolution Radar Imaging*, Artech House, Dedham, MA, 1981.
2. Chen, C. C., and H. C. Andrews, "Target motion induced radar imaging," *IEEE Transactions on Aerospace and Electronic Systems*, Vol. AES-16, 2-14, Jan. 1980.
3. Ozdemir, C., R. Bhalla, L. C. Trintinalia, and H. Ling, "ASAR-Antenna synthetic aperture radar (ASAR) imaging," accepted for publication in *IEEE Trans. Antennas Propagat.*, June 1998.
4. Ling, H., R. Chou, and S. W. Lee, "Shooting and bouncing rays: calculating the RCS of an arbitrary shaped cavity," *IEEE Trans. Antennas Propagat.*, Vol. AP-37, 194-205, Feb. 1989.
5. Baldauf, J., S. W. Lee, L. Lin, S. K. Jeng, S. M. Scarborough, and C. L. Yu, "High frequency scattering from trihedral corner reflectors and other benchmark targets: SBR versus experiment," *IEEE Trans. Antennas Propagat.*, Vol. AP-39, 345-1351, Sept. 1991.
6. Lee, S. W., "Users manual for APATCH," version 1.0, DEMACO, Inc., Champaign, IL, Oct. 1992.
7. Bhalla, R., and H. Ling, "Image-domain ray-tube integration formula for the shooting and bouncing ray technique," *Radio Sci.*, Vol. 30, 1435-1444, Oct.-Sept. 1995.
8. Ozdemir, C., R. Bhalla, and H. Ling, "Fast ASAR image formation using the shooting and bouncing ray technique," *IEEE Antennas Propagat. Soc. Int. Symp.* Vol. 4, 2605-2608, July 1997, Montreal, Canada.
9. Sullivan, T. D., "A technique of convolving unequally spaced samples using fast Fourier transforms," Sandia National Laboratories, SAND89-0077, Jan. 1990.
10. Bhalla, R., and H. Ling, "Three-dimensional scattering center extraction using the shooting and bouncing ray technique," *IEEE Trans. Antennas Propagat.* Vol. AP-44, 1445-1453, Nov. 1996.
11. Bhalla, R., J. Moore, and H. Ling, "A global scattering center representation of complex targets using the shooting and bouncing ray technique," *IEEE Trans. Antennas Propagat.* Vol. AP-

- 45, 1850-1856, Dec. 1997.
12. Segalovitz, A., and B. D. Frieden, "A 'CLEAN'-type deconvolution algorithm," *Astron. Astrophys.*, Vol. 36, 543-556, Apr. 1988.

**Caner Ozdemir** was born in Edremit, Turkey on March 29, 1971. He received the B.S.E.E. degree, in 1992, from the Middle-East Technical University (METU), Ankara, Turkey, and the M.S. and Ph.D. degrees in Electrical Engineering from the University of Texas, at Austin in 1995 and 1998, respectively. From 1992 to 1993, he worked as a project engineer at the Electronic Warfare office of the Turkish Military Electronics Industries (ASELSAN), Ankara, Turkey. From 1995 to 1998, he worked as a research assistant at the University of Texas, at Austin. He is currently with Allied Signals, Columbia, MD. His primary research interests are radar signal processing, electromagnetic scattering and computational electromagnetics.

**Hao Ling** was born in Taichung, Taiwan, on September 26, 1959. He received the B.S. degrees in electrical engineering and physics from the Massachusetts Institute of Technology, in 1982, and the M.S. and Ph.D. degrees in electrical engineering from the University of Illinois at Urbana-Champaign, in 1983 and 1986, respectively. He joined the faculty of the University of Texas at Austin in September 1986 and is currently a Professor in the Department of Electrical and Computer Engineering and holder of the Chevron Centennial Fellowship in Engineering. In 1982, he was associated with the IBM Thomas J. Watson Research Center, Yorktown Heights, NY, where he conducted low temperature experiments in the Josephson Program. While in graduate school at the University of Illinois, he held a research assistantship in the Electromagnetics Laboratory as well as a Schlumberger Fellowship. He participated in the Summer Visiting Faculty Program in 1987 at the Lawrence Livermore National Laboratory. In 1990, he was an Air Force Summer Fellow at the Rome Air Development Center, Hanscom Air Force Base. His research interests in electromagnetic scattering include radar cross section prediction and backscattered signature analysis for scattering mechanism interpretation and target identification applications. Dr. Ling is a recipient of the National Science Foundation Presidential Young Investigator Award in 1987 and the NASA Certificate of Appreciation in 1991.

# RADIATION CENTER REPRESENTATION OF ANTENNA SYNTHETIC APERTURE RADAR (ASAR) IMAGES

Caner Ozdemir\*, Rajan Bhalla and Hao Ling  
Department of Electrical and Computer Engineering  
The University of Texas at Austin  
Austin, TX 78712-1084

## 1 - Introduction

It is well known that antenna characteristics can be dramatically affected by the presence of platforms that support the antenna structure. Recently, we have introduced an imaging algorithm called Antenna Synthetic Aperture Radar (ASAR) that images the locations of the dominant scattering off the platform from antenna radiation data [1]. Such information is useful to the antenna designer in understanding the cause-and-effect relationship in platform scattering. In this work, we will present a sparse representation of platform scattering by extracting a point scatterer representation of the ASAR image. Similar to an ISAR image, an ASAR image exhibits strong point-scatterer like behavior. In the ISAR case, these points are called scattering centers [2]. In our case, we call them *radiation centers* since they are in fact the secondary point radiators on the platform. First, we will use the well-known CLEAN [3] algorithm to extract the radiation centers. Next, we will show that we can reconstruct and extrapolate the antenna radiation data in frequency and aspect with good fidelity by using the radiation centers. Finally, we will demonstrate that the radiation center information can be used to provide important guidelines for reducing platform effects.

## 2 - Extraction of Radiation Centers

Before presenting the radiation center model for antenna radiation data, we shall first review the ASAR image formation algorithm presented earlier in [1] and provide some motivations for the radiation center model. Using the Shooting and Bouncing Ray (SBR) technique [4], it can be shown that a 3-D ASAR image of the platform can be generated via the expression:

$$\text{ASAR}(x, y, z) \approx \sum_{i \text{ rays}} \beta_i \cdot h(x - x_i, y - y_i, z - z_i) \quad (1)$$

$$\text{where } h(x, y, z) = e^{-jk_0(r+x)} \sin c(\Delta k \cdot x) \cdot \sin c(k_0 \Delta \phi \cdot y) \cdot \sin c(k_0 \Delta \theta \cdot z) \quad (2)$$

In the above expression,  $(x_i, y_i, z_i)$  is the location of the hit point on the target for the  $i$ th ray,  $\beta_i$  is the ray amplitude,  $\Delta k$ ,  $\Delta \phi$ ,  $\Delta \theta$  are the half-bandwidths in the  $k$ -,  $\phi$ - and  $\theta$ -domains, respectively. A key observation from eq. (1) is that we can form the ASAR image using SBR on a ray-by-ray basis directly in the image domain. Each ray contributes to a spot centered about  $(x_i, y_i, z_i)$  in the ASAR image, with the footprint of the spot governed by the 3-D ray spread function  $h$ . Since tens of thousands of rays are traced in the SBR process, this may imply that tens of thousands of point radiators are needed to adequately represent an ASAR image. However, the actual ASAR image of a complex platform is actually quite sparse. This is because the rays interfere with one another to give rise to strong coherent scattering over only a small, localized portion of the target. Therefore, an ASAR image can be accurately represented by only a limited number of radiation centers. We adopt a point radiator model which has exactly the same form as (1) to parameterize the ASAR data:

$$\text{ASAR}(x, y, z) \approx \sum_{n \text{ rad. cntrs}} A_n \cdot h(x - x_n, y - y_n, z - z_n) \quad (3)$$

where  $(x_n, y_n, z_n)$  is the radiation center location and  $A_n$  is its amplitude. To determine these parameters, we apply the image processing algorithm CLEAN which has already been successfully used in scattering center extraction [2]. The CLEAN algorithm iteratively picks out the highest point in the image and removes its point-spread response from the image. The extraction process is iterated until the maximum in the residual image reaches a user-defined

threshold. As an example, we used an airplane model whose CAD file (shown in Fig.1) consists of approximately 8,000 perfectly conducting facets. A dipole antenna is located above the cockpit. The simulation is carried out with a SBR-based code Apatch [5]. Fig. 3(a) shows the resulting 3-D ASAR images at different z-slices. The center frequency is 10 GHz with 0.56 GHz of bandwidth sampled over 64 frequencies. The observation angles are centered about the nose of the airplane and range between  $-1.67^\circ$  and  $1.67^\circ$  in azimuth sampled over 32 points and between  $-0.86^\circ$  and  $0.86^\circ$  in elevation over 8 points. Fig. 3(b) shows the locations of the extracted radiation centers from the 3-D ASAR image of Fig. 3(a) using the 3-D CLEAN algorithm. A total of 150 radiation centers are extracted from the image and their locations are plotted in Fig. 3(b) as small circles. We notice that most of them are concentrated around the  $z=2\text{m}$  cut which corresponds to the top surface of the airplane. The rest are located on the two tails. Fig. 3(c) shows the reconstructed ASAR image from the 150 extracted radiation centers. The agreement between the original image and the reconstructed one is quite good over a dynamic range of 50 dB.

### 3 - Applications:

Two examples of the utilities of the radiation center representation are presented. In the first example, we demonstrate how the radiation center concept can be utilized to create a sparse model of the antenna-platform radiation over frequencies and aspect angles, thus achieving data compression. To fully characterize the antenna-platform radiation pattern for all angles, we need to extract 3-D radiation center models at various angles covering the entire aspect sphere. In our example, we focus only on the azimuth angle. The platform-antenna configuration is the same as before. We have chosen an angular granularity of  $5^\circ$  between the extraction angles of each radiation center set so that we have 72 radiation center sets in total covering the whole  $360^\circ$  azimuth. Each radiation center set consists of 100 radiation centers. The bandwidths used for the extraction of each radiation center set are 0.49 GHz in frequency (with a 10 GHz center frequency),  $2.22^\circ$  in azimuth and  $2.46^\circ$  in elevation. We have reconstructed the azimuth pattern from  $0^\circ$  to  $180^\circ$  by using 72 radiation center sets shown as the dashed line in Fig. 4(a). To test the validity of the model, we have also plotted the original pattern (drawn as solid line) calculated by the Apatch code. Since the antenna pattern on a complex platform is such a rapidly varying function of angle, we expand the  $30^\circ$ - $35^\circ$  region in Fig. 4(b) to better display the fine agreement. Note that the data between  $30^\circ$ - $32.5^\circ$  are reconstructed from one set of radiation centers while those from  $32.5^\circ$  -  $35^\circ$  are reconstructed from another set. The data between  $31.11^\circ$  and  $33.89^\circ$  correspond to extrapolated data based on the nearest-neighbor radiation center model. The overall agreement between the two sets of data are fairly good, even in the extrapolated region. Therefore, the radiation pattern of a complex antenna pattern can be sparsely represented by a radiation center model with good fidelity.

In the second example, we utilize the radiation center representation to carry out a platform effect reduction study. Since the radiation centers pinpoint the locations of the dominant secondary scattering on the platform, one way to mitigate such undesirable effects is to place absorbers at those locations. Using the same example as before, we have identified from the database those radiation centers that contribute more than  $-25\text{dB}$  to the radiated field. Then, by tying each radiation center back to the dominant ray hit mechanism that gave rise to it, we place 403 absorbing facets around the platform. The absorber-coated airplane model is shown in Fig. 2. The dark triangles on the platform correspond to absorbing facets. Fig. 5 shows the azimuth radiation pattern from the platform before and after the absorber coating. We can see that for most of the angles, the scattered field from the platform is under the chosen  $-25\text{ dB}$  level. Therefore, it is possible to suppress platform radiation by selectively coating the platform from the radiation center information.

**Acknowledgments:** This work is supported by the Air Force MURI Center for Computational Electromagnetics under Contract No. AFOSR F49620-96-1-0025 and the Office of Naval Research under Contract No. N00014-98-1-0178.

### References

- [1] C. Ozdemir, R. Bhalla, L. C. Trintinalia, and H. Ling, "ASAR - Antenna synthetic aperture radar imaging," submitted for publication in *IEEE Trans. Antennas Propagat.*, Dec. 1996.

- [2] R. Bhalla and H. Ling, "Three-dimensional scattering center extraction using the shooting and bouncing ray technique," *IEEE Trans. Antennas Propagat.*, vol. AP-44, pp. 1445-1453, Nov. 1996.
- [3] W. P. Yu, L. G. To, and K. Oii, "N-point scatterer model RCS/glint reconstruction from high-resolution ISAR target imaging," *Proc. End Game Meas. Modeling Conf.*, pp. 197-212, Point Mugu, CA, Jan. 1991.
- [4] H. Ling, R. Chou and S. W. Lee, "Shooting and bouncing rays: calculating the RCS of an arbitrary shaped cavity," *IEEE Trans. Antennas Propagat.*, vol. AP-37, pp. 194-205, Feb. 1989.
- [5] S. W. Lee, "User's manual for APATCH," version 1.0, DEMACO, Inc., Champaign, IL, Oct. 1992.



Figure 1. View of the platform CAD model with a small dipole placed above cockpit.



Figure 2. The CAD model of the absorber-coated airplane.

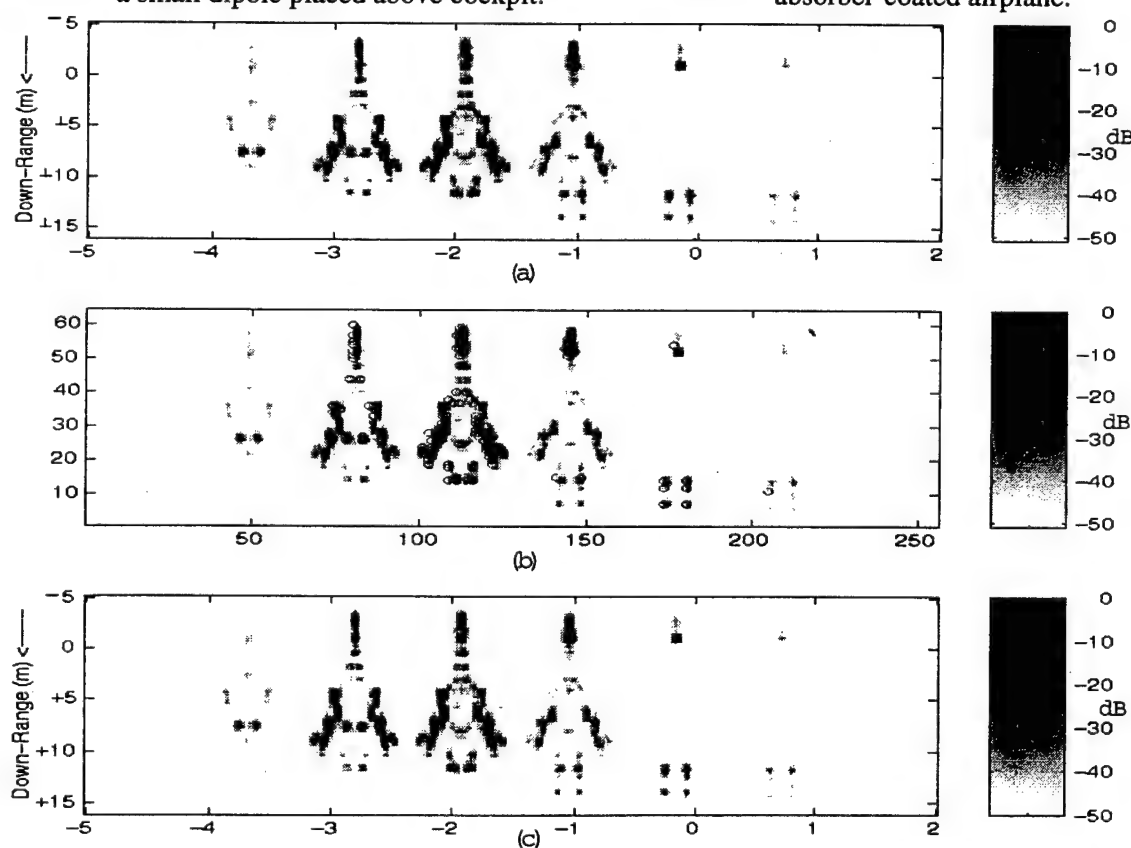


Figure 3. (a) 3-D ASAR image of the airplane generated from the simulated data about nose using the Apatch code. (b) The location of the 150 radiation centers extracted using CLEAN. (c) Reconstructed 3-D ASAR image using the extracted radiation centers.

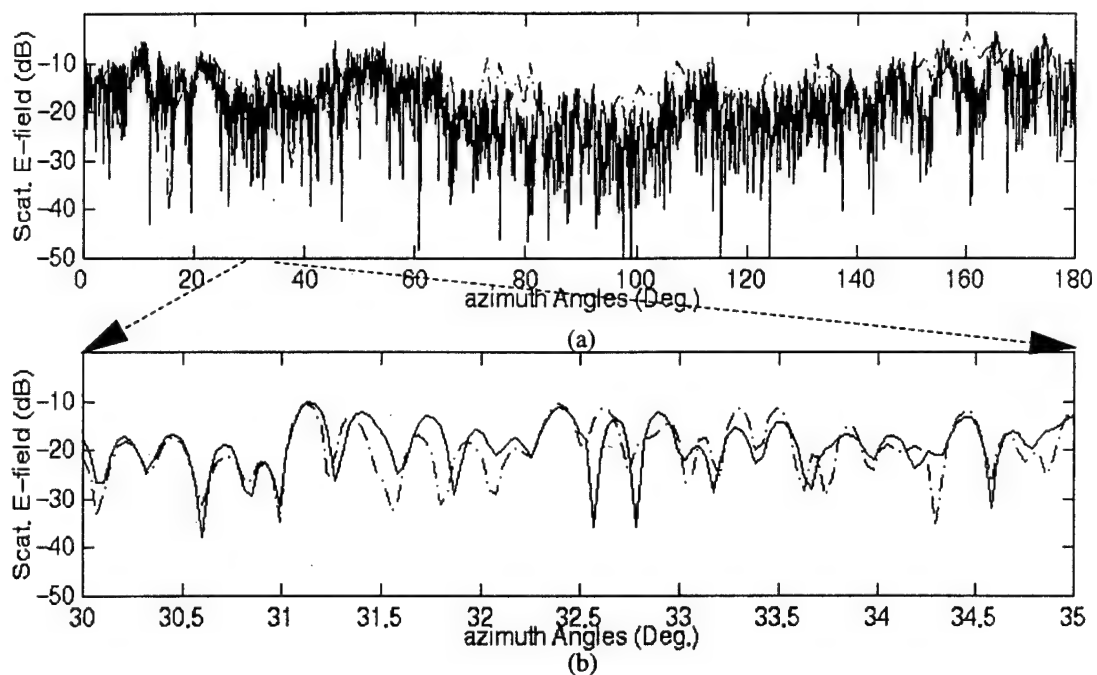


Figure 4. Comparison of the azimuth radiation patterns from the original data (dashed) and the reconstructed data (solid) based on radiation centers. (a) Coarse comparison between  $0^\circ$  and  $180^\circ$ . The original data are sampled at  $1^\circ$  while the reconstructed one are sampled at  $0.07^\circ$ . (b) Detailed comparison between  $30^\circ$  and  $35^\circ$  at the same angular granularity.

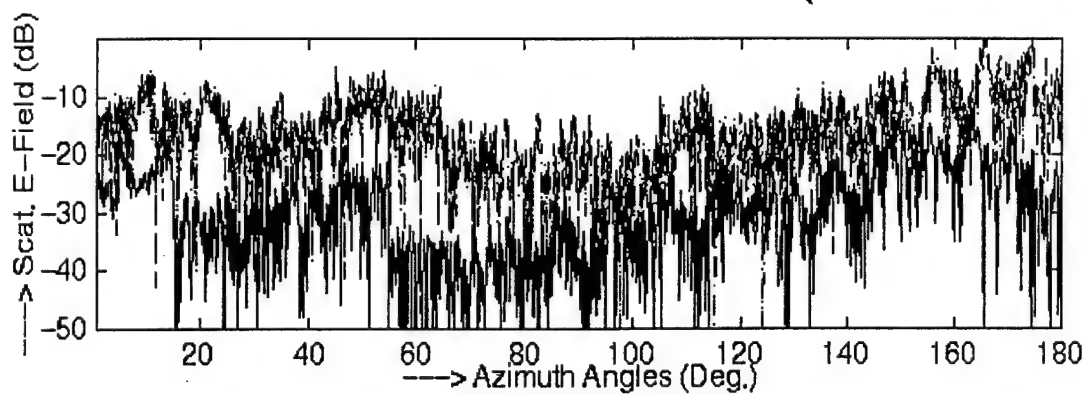


Figure 5. Azimuth radiation patterns before (dashed) and after (solid) putting the absorbers on the platform.



# SYNTHETIC APERTURE RADAR IMAGING ALGORITHM FOR ANTENNA COUPLING

Caner Ozdemir\* and Hao Ling  
Department of Electrical and Computer Engineering  
The University of Texas at Austin  
Austin, TX 78712-1084

## 1. Introduction

The electromagnetic coupling between antennas on a complex platform is an important issue in antenna design. In this work, we set out to develop an imaging algorithm to pinpoint those locations on the platform that give rise to antenna interactions based on the coupling data between antennas. Our approach to this problem is based on the Inverse Synthetic Aperture Radar (ISAR) concept. ISAR imaging is a standard technique to map the locations of dominant scattering off a target based on the multi-frequency, multi-aspect backscattered data [1]. We have already extended this concept to the far-field antenna radiation problem by introducing the Antenna SAR (ASAR) imaging concept [2]. By collecting the multi-frequency, multi-aspect radiation data from an antenna in the presence of the platform, we showed that it is possible to image the locations of the dominant secondary radiation off the platform. In this paper, we will further extend this concept to the near-field antenna coupling problem by constructing the Antenna Coupling SAR (ACSAR) image of the platform. We will show that a platform image can be generated by processing multi-frequency, multi-spatial radiation data about a receiver location from a transmitting antenna. Examples of the ACSAR image will be presented by using the computed data from the Shooting and Bouncing Ray (SBR) code Apatch [3,4]. In addition, we will present a fast algorithm for ACSAR image formation that is specifically tailored to the SBR technique. By taking advantage of the ray tracing information within the SBR engine, we will show that the ACSAR image can be formed with little additional computation time than simple ray tracing.

## 2. ACSAR Imaging Algorithm

We assume the transmitter and receiver setup as depicted in Fig. 1. The electric field at the receiver site due to the scattering from the antenna-platform interaction at point  $P(x_i, y_i, z_i)$  can be written as

$$E_s(k) = A_i \cdot e^{-jkR_{1i}} \cdot e^{-jkR_{2i}} \quad (1)$$

where  $A_i$  is the strength of the scattered field,  $R_{1i}$  is the path length from transmitter antenna to  $P$ ,  $R_{2i}$  is the path length from  $P$  to the receiver location and  $k$  is the free-space wave number. Next, we assume that the radiation data are collected within a certain frequency bandwidth and on a two-dimensional aperture around the receiver point  $(x_o, 0, 0)$ . If the frequency bandwidth is small compared to the center frequency and the aperture around point is small compared to the path length  $R_{2i}$ , we can approximate the received field as a function of frequency and space as follows:

$$E_s(k, y, z) \approx A_i \cdot e^{-jk(R_{1i} + R_{2i})} \cdot e^{-jk y_o \cdot y \cos \alpha_i} \cdot e^{-jk z_o \cdot z \sin \alpha_i \sin \beta_i} \quad (2)$$

In the above formula, it is obvious that there is a Fourier transform relationship between the variables  $(k, y, z)$  and  $(R_i = R_{1i} + R_{2i}, u_i = k_o y \cos \alpha_i, v_i = k_o z \sin \alpha_i \sin \beta_i)$ . Hence by taking the 3-D inverse Fourier transform of the scattered field with respect to  $k, y$ , and  $z$ , we obtain an 3-D image:

$$\text{ACSAR}(R, u, v) = A_i \cdot \delta(R - R_i) \cdot \delta(u - u_i) \cdot \delta(v - v_i) \quad (3)$$

Note that the scattering point P on the platform will manifest itself as a peak in the ACSAR image at  $(R_i, u_i, v_i)$  with amplitude  $A_i$ . It is straightforward to transform the image from the  $(R, u, v)$  coordinates to the desired  $(x, y, z)$  coordinates of the platform. Therefore, by taking the 3-D inverse Fourier transform of the multi-frequency, multi-spatial scattered field data about the receiver location and carrying out the coordinate transformation, it is possible to construct a 3-D image of the platform that displays the strength of the platform scattering.

As an example, we use a test object 'slicy' whose CAD geometry is shown in Fig. 2. The platform is assumed to be perfectly conducting. A half-wave dipole is used as the transmitter. A total of 32 frequencies are computed within a 0.19 GHz bandwidth at the center frequency of 10 GHz. The simulation is carried out by an SBR-based code Apatch [4]. The scattered field is collected on an aperture centered at (35,0,0). There are  $32 \times 32 = 1024$  spatial points on the aperture, ranging from -0.49m to 0.49m in z and from -1.14m to 1.14m in y. In the computed data, we include only the scattered field from the platform and not the primary radiation due to the antenna in the absence of the platform. The resulting 3-D ACSAR image is generated. It is then projected into three 2-D projected views along the 3 principal planes shown in Fig. 3a. We observe in the image the dominant scattering point is around (17.5, -40, 0) which is the specular point between the transmitter and the receiver. We also observe other scattering mechanisms on the top surface of the platform, around the step region of the platform and at the top of the tall cylinder.

### 3. Fast ACSAR Image Formation Using SBR

The ACSAR image formation outlined in the last section requires input data set over multiple frequencies and spatial locations. In this section, we will derive a fast imaging algorithm specially tailored for the SBR approach. It utilizes the ray information available within the ray tracing engine to generate the ACSAR image directly on a ray-by-ray basis without resorting to the expensive multi-frequency, multi-spatial calculations. This approach is similar to the fast image formation algorithm we have developed previously for ISAR and ASAR image simulation [5, 6]. In applying the SBR technique to the antenna radiation problem, rays are first shot from the phase center of the transmitter and traced according to geometrical optics. At the exit point of each ray before they leave the platform altogether, a ray-tube integration is carried out to find the contribution of each ray to the near-field at the receiver. Under this construct, the scattered near field can be written as;

$$E_s(k, y, z) = \sum_{i \text{ rays}} \sigma_i \cdot e^{-jk(R_{1i} + R_{2i})} \cdot e^{-jk_o \cdot y \cos \alpha_i} \cdot e^{-jk_o \cdot z \sin \alpha_i \sin \beta_i} \quad (4)$$

This equation obtained by assuming the bandwidth and the aperture is small and the platform is perfectly conducting.  $\sigma_i$  is proportional to the field at the exit ray-tube, and is only weakly dependent on the frequency and variations on the path length  $R_{2i}$ . Substituting (4) in to our ACSAR formula and performing the 3D inverse Fourier transform operation, we get:

$$\begin{aligned} \text{ACSAR}(R, u, v) &= \text{IFT}_3 \left\{ \sum_{i \text{ rays}} \sigma_i \cdot e^{-jk(R_{1i} + R_{2i})} \cdot e^{-jk_o \cdot y \cos \alpha_i} \cdot e^{-jk_o \cdot z \sin \alpha_i \sin \beta_i} \right\} \\ &= \sum_{i \text{ rays}} \rho_i \cdot h(R - R_i, u - u_i, v - v_i) \end{aligned} \quad (5a)$$

where

$$h(R, u, v) = e^{-jk_o R} \sin c(\Delta k \cdot R) \cdot \sin c(\Delta y \cdot u) \cdot \sin c(\Delta z \cdot v) \quad (5b)$$

In (5b),  $\Delta k$ ,  $\Delta y$ ,  $\Delta z$  are respectively the half bandwidth in frequency and the half widths of the aperture. We can rewrite the last equation as a convolution between a 3-D weighted impulse train and the ray spread function h:

$$\text{ACSAR}(R, u, v) = \left( \sum_{i \text{ rays}} \rho_i \cdot \delta(R - R_i, u - u_i, v - v_i) \right) * h(R, u, v) = g * h \quad (6)$$

The above convolution can be computed quickly using an interpolation algorithm and FFT [5, 6].

We have applied the fast approach to the same geometry. An oversampling ratio of 4 is used in the interpolation grid to ensure the accuracy in the computation. The results are depicted in Fig. 3b as three 2-D projected ACSAR images. By comparing these images with the images that are generated by using the standard frequency-aperture approach, we observe a fairly good agreement. To show the time savings that we have gained by using the fast algorithm, we list the computation times in Table 1. The ray-tracing time of 9 minutes is the same for both approach; however, the ray summation time takes about 106 hours in the frequency-aperture approach. On the other hand, the fast approach reduces the ray summation time is to only 6 minutes. Consequently, the combination of SBR and the fast ACSAR technique can be used as a CAD tool for diagnosing platform effects.

**Acknowledgments:** This work is supported by the Air Force MURI Center for Computational Electromagnetics under Contract No. AFOSR F49620-96-1-0025 and the Office of Naval Research under Contract No. N00014-98-1-0178.

### References

- [1] D. L. Mensa, *High Resolution Radar Imaging*. Artech House, Dedham, MA, 1981.
- [2] C. Ozdemir, L. C. Trintinalia and H. Ling, "Antenna synthetic aperture radar (ASAR) image formation," *IEEE Antennas Propagat. Soc. Int. Symp.*, pp. 2601-2604, vol.4, July 1997, Montreal, Canada.
- [3] H. Ling, R. Chou and S. W. Lee, "Shooting and bouncing rays: calculating the RCS of an arbitrary shaped cavity," *IEEE Trans. Antennas Propagat.*, vol. AP-37, pp.194-205, Feb. 1989.
- [4] S. W. Lee, "Users manual for APATCH," version 1.0, DEMACO, Inc., Champaign, IL, Oct. 1992.
- [5] R. Bhalla, and H. Ling, "Image-domain ray-tube integration formula for the shooting and bouncing ray technique," *Radio Sci.*, vol. 30, pp. 1435-1444, Oct.-Sept. 1995.
- [6] C. Ozdemir, R. Bhalla and H. Ling, "Fast ASAR image formation using the shooting and bouncing ray technique," *IEEE Antennas Propagat. Soc. Int. Symp.*, pp. 2605-2608, Vol.4, July 1997, Montreal, Canada.

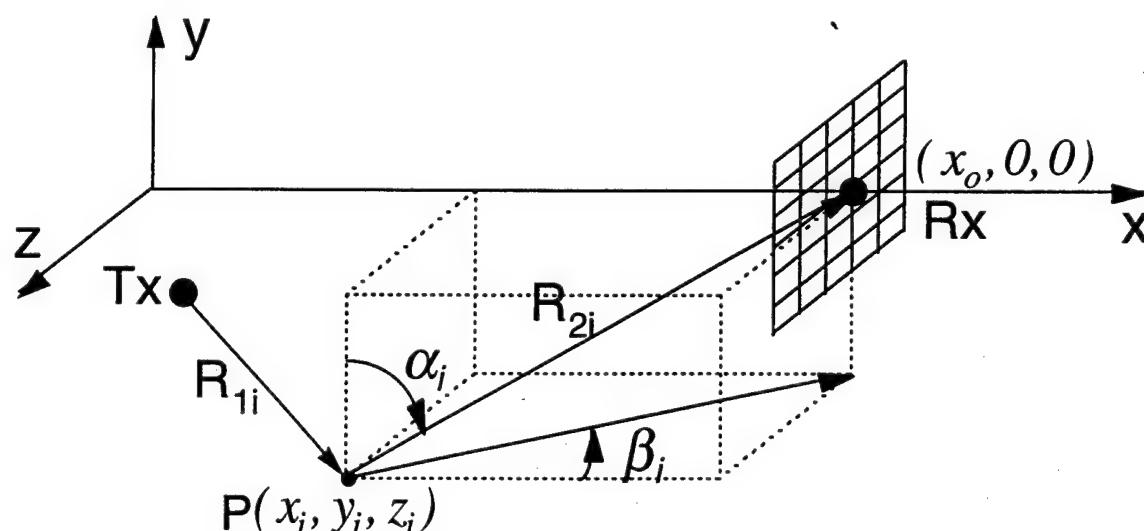


Figure 1. The path of a radiated signal that is scattered off a point on the platform.

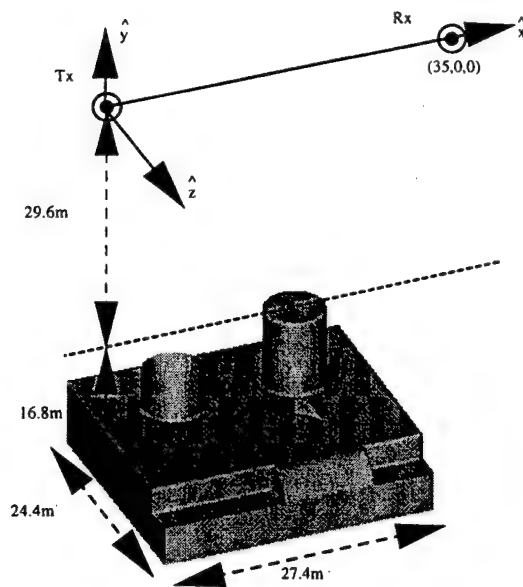


Figure 2. The view of the test object under consideration.

	Freq-Aperture Approach	Fast Algorithm
Ray Summation Time	160.52 hrs	6 minutes
Ray Tracing Time	9 minutes	9 minutes
Total Time	160.67 hrs	15 minutes

Table 1. The computation times for the test object on an IBM RS-6000 /590 workstation

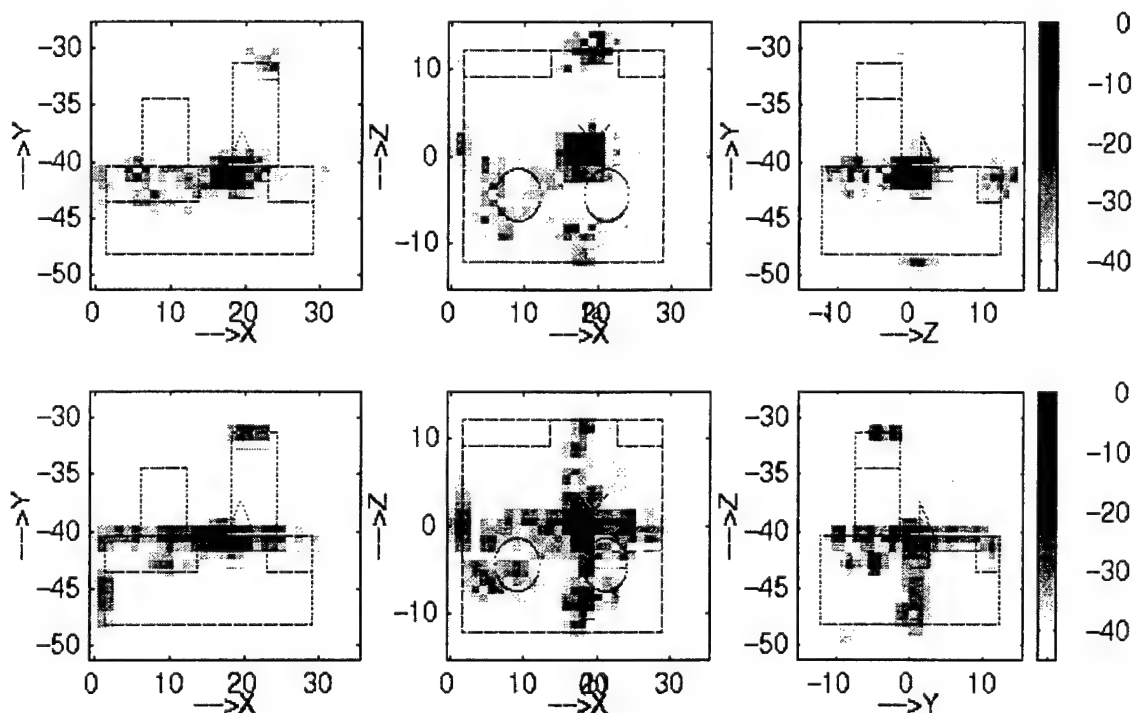


Figure 3. Comparison of the 2-D projected ACSAR images using (a) frequency-aperture approach, (b) fast approach.

## RADAR SIGNATURE EXTRAPOLATION FOR FISC

Yuanxun Wang\* and Hao Ling  
Department of Electrical and Computer Engineering  
University of Texas at Austin  
Austin, Texas 78712-1084

Jiming Song and Weng Cho Chew  
Department of Electrical and Computer Engineering  
University of Illinois  
Urbana, Illinois 61801

### I. Introduction

Moment method is one of the most popular frequency domain simulation methods in computational electromagnetics (CEM). Since it solves an integral equation rigorously through boundary discretization, huge computer memory and computation time are needed to simulate the scattering phenomena for targets of large electrical sizes. Recently the development of the fast multipole method (FMM) and the multilevel fast multipole algorithm (MLFMA) has led to the reduction of the computational complexity of the matrix-vector multiplication operation in moment method from  $O(N^2)$  to  $O(N^{1.5})$  or  $O(N\log N)$  [1,2]. The FLFMA-based code FISC [3] is now capable of computing the radar cross section (RCS) of a full-size fighter airplane at 1 GHz on a workstation in several hours of run time. While such an advance in computational capability has brought much excitement to the CEM community, real-world radar signature prediction often requires that the same calculation be repeated over many frequencies and aspect angles. For example, in automatic target identification applications, range profiles of the target are commonly used to pinpoint target features. To generate range profiles requires hundreds of frequency calculations that make the computation time still extraordinarily long even using FISC. In this paper, we present a frequency extrapolation scheme to speed up the signature prediction procedure using FISC by avoiding such exhaustive computations.

We adopt a model-based approach [4-6] to the frequency extrapolation problem. The key in the success of an extrapolation algorithm is a good model of the physical observable to be extrapolated. Here, we propose a scheme that parameterizes the current on the target, which is available in the FISC solution, based on a multipath excitation model. We first run FISC for the scattering problem at several frequency points, then apply the ESPRIT superresolution algorithm [7] directly to the induced current output at these frequency points to extract the time-of-arrival and amplitude parameters. Once these parameters are obtained, the frequency dependent model of the induced current on each facet of the target can be constructed. Thus the induced currents over the whole frequency band can be extrapolated and the multifrequency far field can be calculated. The range profiles of a low-Q missile model are calculated as an example to demonstrate the performance of the algorithm.

### II. Model-Based Parameterization

We assume the following frequency dependent model for the induced current on the target:

$$J(f, S) = \sum_{i=1}^N A_i(S) \exp[-j2\pi f t_i(S)] \quad (1)$$

where  $f$  is the frequency,  $S$  represents the position on the target surface, and  $(A_i, t_i)$  are respectively the amplitude and time-of-arrival of the  $i$ th scattering mechanism observed at  $S$ . This is a physical model consistent with high-frequency electromagnetic phenomenology. For example, for a point on the target surface in the lit region of the incident wave, the first term of the expansion should correspond to the physical optics current. The higher order terms correspond to multiple scattering effects such as currents induced by multiple reflected or diffracted fields that have longer time-of-arrival. In our model, we assume  $A_i$  to be independent of frequency.

With this model in hand, we next extract the parameters  $(A_i, t_i)$  from a limited number of frequency calculations based on FISC at each point on the target. We apply the superresolution algorithm ESPRIT for this purpose due to its robustness in the presence of noise. ESPRIT is based on the data model:

$$F(f_m) = \sum_{i=1}^N A_i e^{-j2\pi f_m t_i} + n(f_m) \quad , \quad f_m = f_1, f_2, \dots, f_M \quad (2)$$

where  $n(\bullet)$  denotes additive white Gaussian noise. If the data sequence obeys this ideal model and the number of the sampling points  $M > 2N+1$ , ESPRIT can estimate  $N$  and resolve each  $A_i$  and  $t_i$ . Of course, for real CEM data, the nature of the noise is more complex and will degrade the performance of the algorithm. At frequencies sufficient above target resonances, the first few interactions dominate the scattering phenomenon and only a small  $N$  is needed to adequately model the observed data. Therefore by running ESPRIT using the FISC generated current at  $M$  frequencies, the frequency-dependent current model in (1) can be obtained. Note that the ESPRIT processing is carried out at each point on the target. Once such a model is found, we can extrapolate the data to determine the currents at other frequencies. The total scattered field versus frequency can thus be calculated by integrating the extrapolated currents.

Two comments are in order. First, just as in Fourier processing, the maximum unambiguous time delays that can be resolved by ESPRIT is inversely proportional to the frequency sampling of the data points. Therefore, the frequency sampling must be chosen sufficiently small to avoid aliasing in the time-of-arrival estimates. Typically, we choose the frequency sampling to allow a range window that is at least twice the size of the target. Second, we have adopted the time-of-arrival model for the induced current in our extrapolation scheme. The same model can also be applied directly to the total scattered field. This is commonly known as the scattering center model. However, we have found that the scattered field requires far more terms to model adequately for a complex target. This means that a far larger number of frequency points are needed from FISC simulation to achieve a good frequency extrapolation model.

### III. Numerical Results

To demonstrate the performance of our extrapolation algorithm, the frequency response and range profile of a missile model are computed as an example. The length of the target is about 50 inches and the model consists of 5679 perfectly conducting facets (see Fig. 1). The brute-force frequency data are first generated at 30° in azimuth and 0° in elevation over a frequency band from 2 GHz to 6 GHz. The frequency sampling interval is 0.05 GHz and thus a total of 81 frequency

points are computed. To test the extrapolation algorithm, 10 frequency points between 2.50 GHz and 2.95 GHz from FISC are used to extrapolate the scattered fields to other frequencies using a model with  $N=4$ . The frequency response of the scattered fields for the VV polarization is plotted in Fig. 2. We see that the extrapolated far fields agree quite well with the data directly computed using FISC within the frequency range 2.5 to 4.5 GHz. Discrepancies in amplitude occur outside of this range. However, note that the peak and null positions of the original data are still fairly well reproduced by the extrapolation. This indicates a good time-of-arrival estimate and the discrepancy is more likely due to the frequency dependent amplitude effects which are not included in the present model. Since only ten frequency points near the low frequency end are computed, such an algorithm leads to large computational savings. The total computation time (including post-processing) for FISC with extrapolation is about 3 hours in an SGI O2 workstation (R10K/155MHz), while it takes about 80 hours on the same machine for the brute-force frequency calculations. Fig. 3 is the range profile comparison obtained by Fourier transforming the frequency response. We see that the main scattering features of the extrapolated results coincide very well with the reference results. Fig. 4 shows the comparison of the extrapolated range profile against the reference result for the HH polarization. Again, good agreement for the dominant scattering features is observed. The theoretical and practical limitation of this extrapolation algorithm is currently under study. We will also report on the extension of this concept in simulating two-dimensional radar imagery of complex targets.

#### Acknowledgments

This work is supported by the Air Force MURI Center for Computational Electromagnetics under Contract No. AFOSR F49620-96-1-0025, and the Office of Naval Research under Contract No. N00014-98-1-0178.

#### References

- [1] R. Coifman, V. Rokhlin, and S. Wandzura, "The Fast Multipole Method for the Wave Equation : A Pedestrian Prescription," *IEEE Trans. Antennas Propagat. Mag.*, Vol. 35, No. 3, pp. 7-12, June 1993.
- [2] J. Song, C. C. Lu and W. C. Chew, "Multilevel Fast Multipole Algorithm for Electromagnetic Scattering by Large Complex Objects," *IEEE Trans. Antennas Propagat.*, vol. AP-45, pp.1488-1493, Oct. 1997.
- [3] User's Manual for FISC (Fast Illinois Solver Code), Center for Computational Electromagnetics, University of Illinois at Urbana-Champaign and DEMACO, Inc., Champaign, IL, Jan. 1997.
- [4] G. J. Burke, E. K. Miller, S. Chakrabarti and K. Demarest, "Using Model-Based Parameter Estimation to Increase the Efficiency of Computing Electromagnetic Transfer Functions," *IEEE Trans. Magnetism*, vol. 25, pp. 2807-2809, July 1989.
- [5] K. Kottapalli, T. K. Sarkar, Y. Hua, E. K. Miller, and G. L. Burke, "Accurate Computation of Wide-Band Response of Electromagnetic Systems Utilizing Narrow-Band Information," *IEEE Trans. Microwave Theory Tech.*, vol. MTT-39, pp.682-687, Apr. 1991.
- [6] Z. Altman and R. Mittra, "Combining an Extrapolation Technique with the Method of Moments for Solving Large Scattering Problems Involving Bodies of Revolution," *IEEE Trans. Antennas Propagat.*, vol. AP-44, pp. 548-553, Apr. 1996.
- [7] R. Roy, A. Paulraj, and T. Kailath, "ESPRIT - A Subspace Rotation Approach to Estimation of Parameters of Cisoids in Noise," *IEEE Trans. Acoust., Speech, Signal Processing*, vol. ASSP-34, pp. 1340-1342, Oct. 1986.



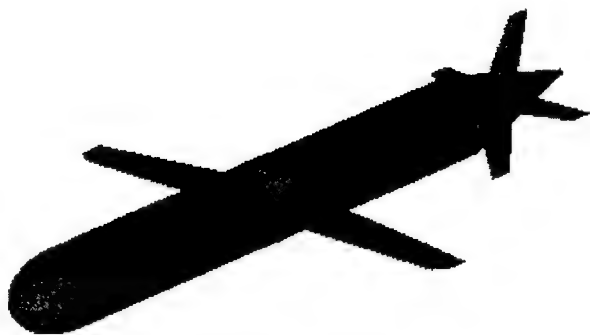


Fig.1 The outlook of the missile model.

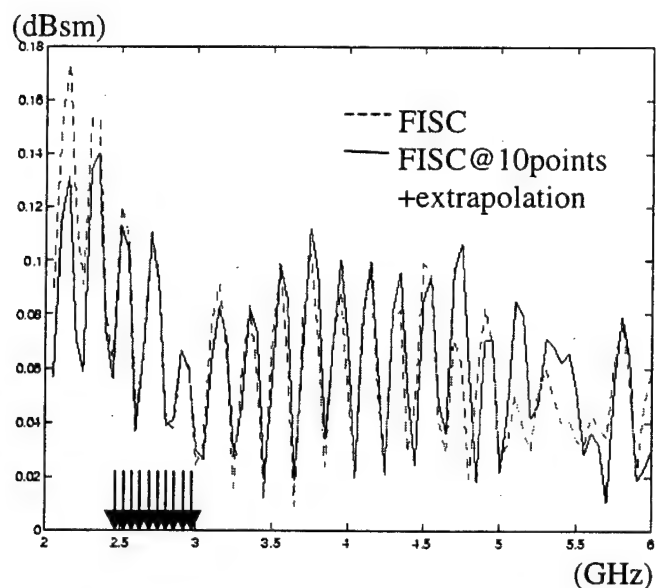


Fig.2. Comparison of the backscattered field versus frequency between the brute-force FISC results and the extrapolation results for the VV polarization.

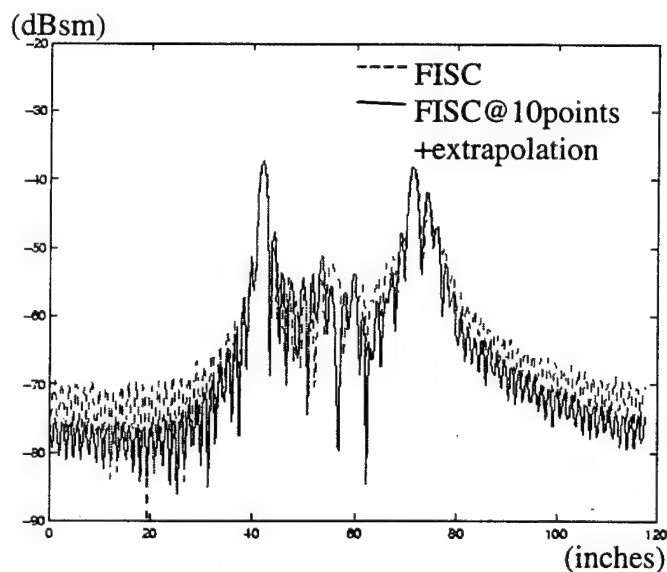


Fig.3. Comparison between the range profiles for the VV polarization obtained by Fourier transforming the frequency response in Fig.2.

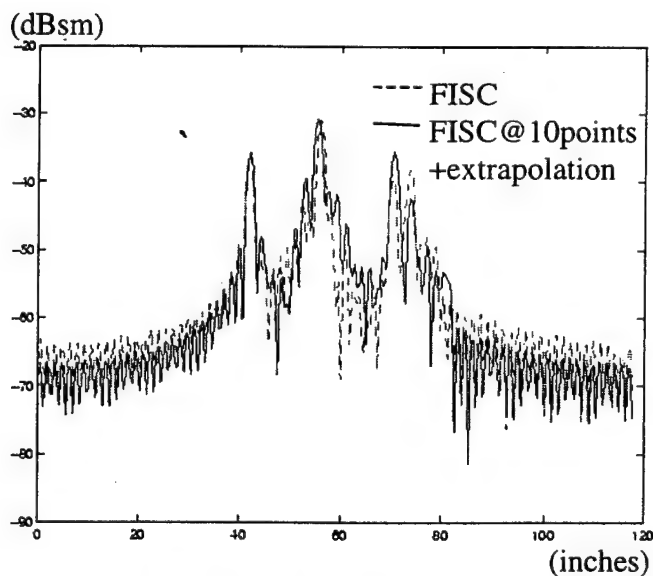


Fig.4. Comparison between the range profiles for the HH polarization obtained by brute-force FISC and FISC + extrapolation.



## Determining the Equivalent Impedance Boundary Condition for Material-Coated Corrugated Gratings Based on the Genetic Algorithm

Tao Su\* and Hao Ling  
Department of Electrical and Computer Engineering  
The University of Texas at Austin  
Austin, TX 78712

### I. Introduction

The impedance boundary condition (IBC) approximation is an effective way to model complex structures [1-3]. It replaces the original structure with a surface impedance so that the problem dimension is reduced by one. In large-scale problems such as the scattering from a 3-D target coated with absorbing materials, the IBC approach will result in large savings in computer resources since the fine details of the structure are replaced by simple impedance boundary conditions on the surface. In this paper, we set out to determine the equivalent IBC model of a material-coated corrugated grating (Fig. 1).

It is not an easy task to find a simple IBC that accurately approximates the original structure over a broad range of incident angles for an arbitrary grating structure. We therefore employ the genetic algorithm (GA) to find the optimal parameters in our IBC model. In our approach, a rigorous solution of the reflection coefficients at a few incident angles is first calculated using a method of moments (MoM) code. The IBC model is used to predict the reflection coefficients at the same observation angles. The model coefficients are then optimized so that the difference between the IBC-predicted and the MoM-predicted reflection coefficients is minimized. The genetic algorithm proves to be quite efficient in obtaining an accurate IBC model. The agreement between the IBC-predicted reflection coefficients and the reference MoM ones are good at most incident angles, even near grazing.

### II. Formulation

In our approach, the reflection coefficients at a number of observation angles are first computed by the method of moments. This solution serves as the reference data for our IBC model. The MoM formulation for a material coated grating, as shown in Fig. 1, begins by dividing one cell of the grating into different homogenous regions according to the material layers. The boundary integral equations are then obtained for each region. Periodic boundary conditions are applied in each region and the fields are matched at the interfaces between regions. Finally, the fields in the top half-space are expanded into a sum of Floquet harmonics and are matched to the fields in the lower region so that the reflection coefficients can be calculated. A detailed description of this method can be found in [4].

Next, we determine the reflection coefficients based on an approximate IBC model. The impedance boundary condition can be written as [1]

$$\begin{bmatrix} E_z \\ E_x \end{bmatrix} = \begin{bmatrix} Z_{zz} & Z_{zx} \\ Z_{xz} & Z_{xx} \end{bmatrix} \begin{bmatrix} H_z \\ H_x \end{bmatrix} \quad (1)$$

Since the structure is periodic, each element of the boundary impedance can be expanded in a Fourier series and the expansion coefficients are the model parameters to be determined. Note that the cross impedance terms  $Z_{xz}$  and  $Z_{zx}$  are kept in our formulation so we can assess their importance. The reflected wave from the periodic structure consists of an infinite number of Floquet harmonics, either propagating or evanescent. By truncating the Floquet harmonics to a finite order and matching fields at the boundary, a matrix equation can be set up for determining the reflection coefficients. This relationship is utilized by the genetic algorithm to evaluate the IBC parameters.

In the final step, the model parameters are optimized by the genetic algorithm. In GA, the parameters to be optimized are first encoded into binary form [5, 6]. A set of the encoded parameters is known as a chromosome. The basic idea of GA is to generate a pool of chromosomes, discard the bad ones, keep the good ones and let them evolve to produce better chromosomes. Each searched chromosome is evaluated by a cost function which, in our case, is the mean square error between the reflection coefficients computed by MoM and those predicted by the IBC model. The evolution process is repeated until the best parameters are found.

Compared with other IBC approaches, the method described above has several advantages. First, the boundary impedance is assumed to be anisotropic so that the same model can be applied to oblique incidence from any angle  $\theta$  and  $\phi$  shown in Fig. 1. Second, it is possible to build in spatial variation of the boundary impedance by adjusting the number of terms used in the Fourier series expansion. By using more terms, the IBC model can be made more accurate. Moreover, the boundary impedance is solved from error minimization by the genetic algorithm. Thus the number of observation points is flexible and can be increased to obtain better results. Most important of all, the position of the impedance surface can also be optimized. In general layered coating problems, there is not a preferred position for the impedance surface. The solution can sometimes be improved by applying the IBC at a position other than a natural interface in the structure [3]. Therefore, by solving for the best position of the impedance surface as one of the model parameters, the accuracy of the model can be improved.

### III. Results

In this section, two examples are presented to demonstrate the effectiveness of the method. The first example is a deep triangular grooved grating with relatively small period. The geometry of one cell of the grating is shown in Fig. 2 (a). The coating material is MagRAM with the material constants  $\epsilon_r = 14.35 - j0.28$  and  $\mu_r = 1.525 - j1.347$  at the frequency of 10 GHz. 17 observation angles are selected which include normal incidence and the combination of  $\theta = 20^\circ, 40^\circ, 60^\circ, 80^\circ$  and  $\phi = 0^\circ, 30^\circ, 60^\circ, 90^\circ$ . In order to compare with the simple tensor impedance boundary condition (TIBC) approach, we set  $Z_{xz}$  and  $Z_{zx}$  in (1) to zero and use only one term in the Fourier expansion for  $Z_{zz}$  and  $Z_{xx}$ . The reflection coefficients of the H-pol and V-pol incidence are plotted in Figs. 3 (a) and 3 (b), respectively. In the figures, the  $x$  axis is divided into sections of different incident angle  $\theta$ , which varies from 5 to 85 degrees in steps of 10 degrees. In each of the  $\theta$  section, the

grating angle  $\phi$  varies from 0 to 90 degrees. In using the TIBC, we put the impedance surface at the conductor backing since it is the only plane in the structure. It is obvious that TIBC is good only when the incident angle  $\theta$  is small, especially for the V-pol incidence. But with the GA approach, the position of the impedance surface is also optimized so that the matching is good even near grazing incidence.

In example 2, we compare the IBC approximations with and without the cross impedance terms  $Z_{xx}$  and  $Z_{zz}$ . The geometry of the structure is shown in Fig. 2 (b). The material constants are  $\epsilon_r = 8.3-j2.4$  and  $\mu_r = 2-j0.9$  at 10 GHz. The same observation points are used as in the previous example. The 0th order IBC is determined and the comparison between the reflection coefficients is illustrated in Fig. 4. With the cross impedance included, the accuracy of the approximation is improved. Further improvement in the accuracy can be achieved by increasing the order of the IBC model.

#### IV. Conclusion

In this paper, an impedance boundary condition model based on the genetic algorithm is proposed to approximate arbitrary coated gratings in scattering problems. The periodic structure is replaced by a periodic IBC on a virtual surface. The boundary impedance and the position of the surface are optimized by matching the reflection coefficients to the rigorous numerical solution at a number of incident angles. Similar to traditional IBC models, this approach is most effective when the coating material is high-loss and of high contrast. Finally, the output IBC model generated by this algorithm can be incorporated into an existing computational electromagnetics code to assess the performance of the corrugated surface when mounted on complex platforms.

#### Acknowledgment

This work is partly supported by the Office of Naval Research under Contract No. N00014-98-1-0178 and the Air Force MURI Center for Computational Electromagnetics under Contract No. AFOSR F49620-96-1-0025.

#### References

- [1] D. J. Hoppe and Y. Rahmat-Samii, *Impedance Boundary Conditions in Electromagnetics*, Bristol: Taylor & Francis, 1995.
- [2] T. B. A. Senior and J. L. Volakis, "Generalized impedance boundary conditions in scattering", *Proc. IEEE*, v 79, n 10, pp 1413-1420, Oct 1991.
- [3] T. B. A. Senior and J. L. Volakis, "Derivation and application of a class of generalized boundary conditions", *IEEE Trans. Antennas Propagat.*, v 37, n 12, pp 1566-1572, Dec 1989.
- [4] J. Moore, H. Ling and C. S. Liang, "The scattering and absorption characteristics of material-coated periodic grating under oblique incidence", *IEEE Trans. Antennas Propagat.*, v 41, n 9, pp 1281-1288, Sept 1993.
- [5] R. L. Haupt, "An introduction to genetic algorithms for electromagnetics", *IEEE Antennas Propagat. Magazine*, v 37, n 2, pp 7-15, Apr 1995.
- [6] D. S. Weile and E. Michielssen, "Genetic algorithm optimization applied to electromagnetics: a review", *IEEE Trans. Antennas Propagat.*, v 45, n 3, pp 343-353, Mar 1997.

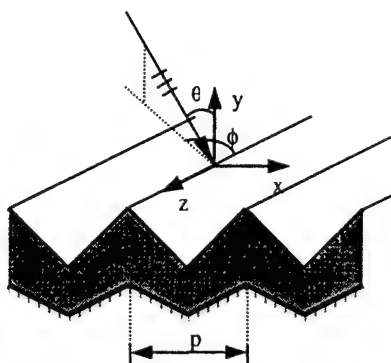


Fig. 1 Problem definition

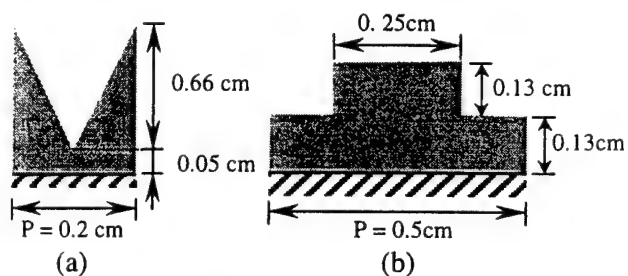
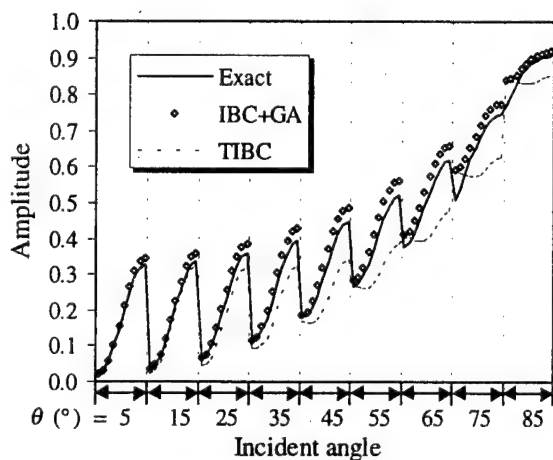
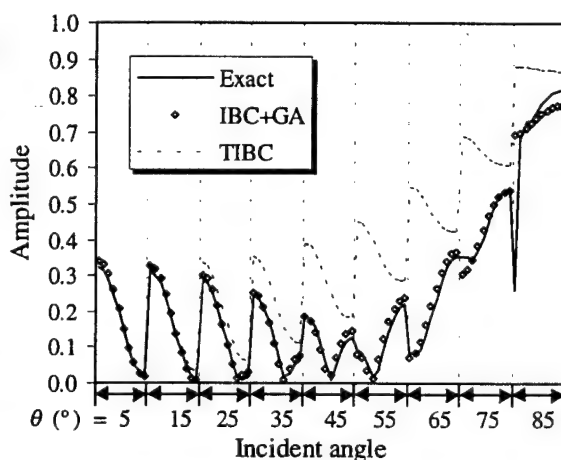


Fig. 2 Some grating geometry

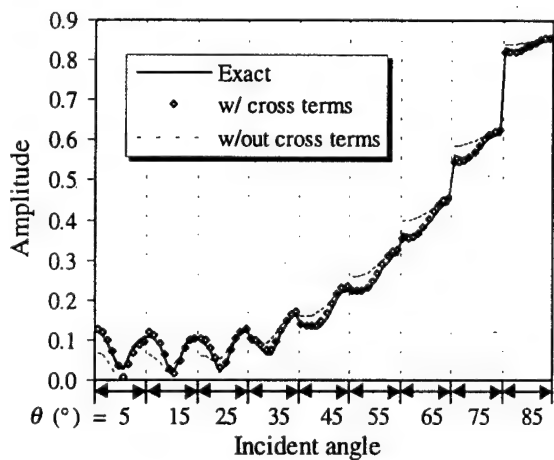


(a) H-H polarization

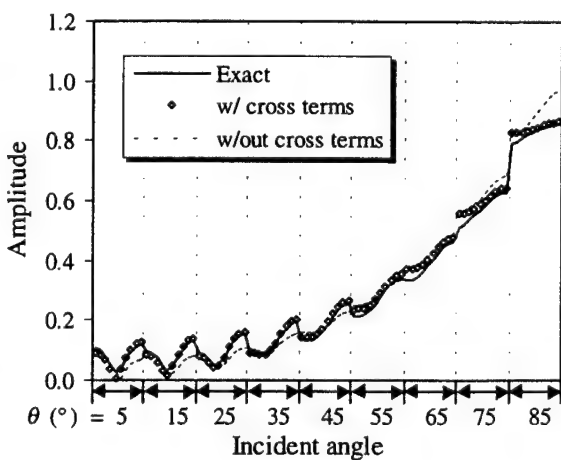


(b) V-V polarization

Fig. 3 Comparison between direct TIBC and GA approach



(a) H-H polarization



(b) V-V polarization

Fig. 4 improvement by considering the cross impedance terms

# Model-Based Frequency Extrapolation of Antenna Radiation Characteristics on Complex Platforms

Tao Su, Yuanxun Wang and Hao Ling  
 Department of Electrical and Computer Engineering  
 The University of Texas at Austin  
 Austin, TX 78712

## I. Introduction

In antenna design and analysis, the mounting platform can have a significant effect on the antenna radiation characteristics. However, rigorous solution of the radiation problem over a complex platform is very time consuming, and the computation complexity increases dramatically as the frequency increases. In this paper, we present a model-based frequency extrapolation technique with which the radiated field over a broad band of frequencies can be obtained using the rigorously computed results at low frequencies.

Our approach entails three steps. First, the induced current on the platform surface is computed at low frequencies using the method of moments (MoM). Second, we apply the time-of-arrival model to the current on each basis element on the surface. The model coefficients are obtained using super-resolution algorithm ESPRIT [1]. Finally, the induced current at higher frequencies is computed using the model and the radiation characteristics are calculated. This approach is similar to that present in [2] and [3] for radar signature extrapolation. Our results show that when the frequencies and the discretization of the platform are properly chosen, the radiated field at higher frequencies can be extrapolated with only moderate computational cost.

## II. Extrapolation Methodology

As the first step of the extrapolation process, the induced current on the target is computed at a small set of points at low frequencies. Once the current over the surface is computed at low frequencies, we apply the time-of-arrival model to each of the current element. In this model, we assume that the total current is induced by different scattering mechanisms, as shown in Fig. 1. Each of the incident mechanism has a distinct arrival time, so that the current can be written as

$$J(\omega) = \sum_{n=1}^N a_n e^{-j\omega t_n} \quad (1)$$

where  $\omega$  is the angular frequency,  $N$  is the total number of incident mechanisms and  $t_n$  is the arrival time of the  $n^{\text{th}}$  incident mechanism.

Since the incident mechanisms correspond to scattering from different parts of the target, the maximum difference in  $t_n$  is related to the size of the target. Thus the sampling rate in the frequency domain should be high enough to distinguish these time events from all parts of the target. Based on this consideration, we approximately constraint the sampling rate in frequency to

$$\Delta f < c/D \quad (2)$$

where  $c$  is the speed of light and  $D$  is the maximum dimension of the target.

The model coefficients  $a_n$  and  $t_n$  are obtained using the superresolution algorithm ESPRIT, which is based on the model that the signal consists of a sum of exponential and additive white noise. Given a sequence with  $M$  samples, the algorithm can estimate the number of exponential  $N$  and determines the amplitude and period of each exponential term. The basic requirement in the number of samples is  $M > 2N + 1$ . Once the model parameters are found, the induced current at higher frequencies can be computed using (1). The radiated field is then easily obtained from the extrapolated current.

### III. Results

As an example, we consider a 2-D structure as shown in Fig. 2 (a). We are interested in the radiation pattern over a frequency band from 0.15 to 0.45 GHz. To obtain the data for the extrapolation, we compute the induced current at 10 frequencies from 0.15 to 0.24 GHz. Then we use the ESPRIT algorithm to obtain the model coefficients for each current element and compute the radiated field based on the model. Fig. 2(a) shows the radiated field of a horizontally polarized line source as a function of frequency at an elevation angle of  $40^\circ$ . The dashed curve is obtained from the model-based extrapolation while the solid curve is the reference brute-force solution. We observe that the extrapolation algorithm correctly predicts the peaks and null positions in frequency, indicating a good estimate on the times-of-arrival. Fig. 2(b) is the time domain response obtained via an inverse Fourier transform of the frequency data. The first large peak corresponds to the specular scattering from the flat surface and the second large peak is due to the scattering from the step region.

We notice from Fig. 2(a) that the model-predicted field matches well with the reference field at the first 10 frequencies, but drops below the computed field as frequency goes higher. This is because the intensity of the field radiated by the line source is proportional to the square root of the frequency. We can overcome this by compensating this effect before doing the extrapolation. Thus the time-of-arrival model becomes

$$J(\omega) = \left( \sum_{n=1}^N a_n e^{-j\alpha_n} \right) \sqrt{\omega} \quad (3)$$

where  $\sqrt{\omega}$  should be replaced by  $\omega$  for 3-D situations. After the compensation, the extrapolation result is further improved, as shown by the frequency and time responses in Figs. 3(a) and 3(b).

Finally we look at the radiation problem of the 3-D platform in Fig. 4(a). The source is a horizontally polarized dipole. The solver used is FISC [4], which is a 3D MoM code based on the fast multipole method. Similar to the 2-D case, we use the computed current at 10 frequencies from 0.15 to 0.24 GHz to extrapolate the data to 0.45 GHz. The extrapolated radiation field as a function of frequency at the elevation angle of  $40^\circ$  is shown in Fig. 4(b) as the dashed curve. The reference brute-force solution is plotted as the solid curve. The major features of the radiated field are well characterized by the extrapolation algorithm.

#### IV. Conclusion and Discussion

As we have seen from the results, the frequency extrapolation technique is an efficient way of obtaining the radiation pattern over a broad band of frequencies. Computation time is reduced dramatically since the current is rigorously solved only at low frequencies. We improved the result by compensating the frequency factor of the source in the time-of-arrival model. This indicates that a wrong frequency dependence in the model may result in errors in the model coefficients. In addition to the frequency factor of the source, the frequency dependence of different scattering components of each current element could be different, due to different scattering physics. Further incorporation of these effects should further enhance the accuracy of the extrapolation.

#### Acknowledgments

This work is supported by the Office of Naval Research under Contract No. N00014-98-1-0178, and in part by the Air Force MURI Center for Computational Electromagnetics under Contract No. AFOSR F49620-96-1-0025.

#### References

- [1] R. Roy, A. Paulraj and T. Kailath, "ESPRIT – a subspace rotation approach to estimation of parameters of cisoids in noise," *IEEE Trans. Acoust., Speech, Signal Processing*, vol. ASSP-34, pp. 1340-1342, Oct. 1986.
- [2] Y. Wang, H. Ling J. Song and W. C. Chew, "A frequency extrapolation algorithm for FISC," *IEEE Trans. Antennas Propagat.*, vol. 45, pp. 1891-1893, Dec. 1997.
- [3] Y. Wang and H. Ling, "Radar signature prediction using moment method codes via a frequency extrapolation technique," submitted to *IEEE Trans. Antennas Propagat.*, Feb. 1998.
- [4] *User's Manual for FISC (Fast Illinois Solver Code)*, Center of Computational Electromagnetics, Univ. of Illinois, Champaign, IL, and DEMACO, Inc., Champaign, IL, Jan. 1997.

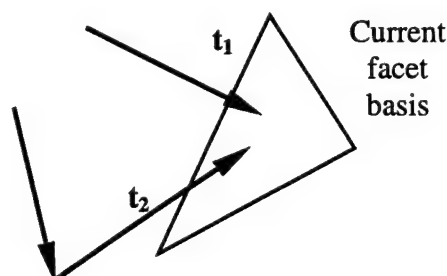
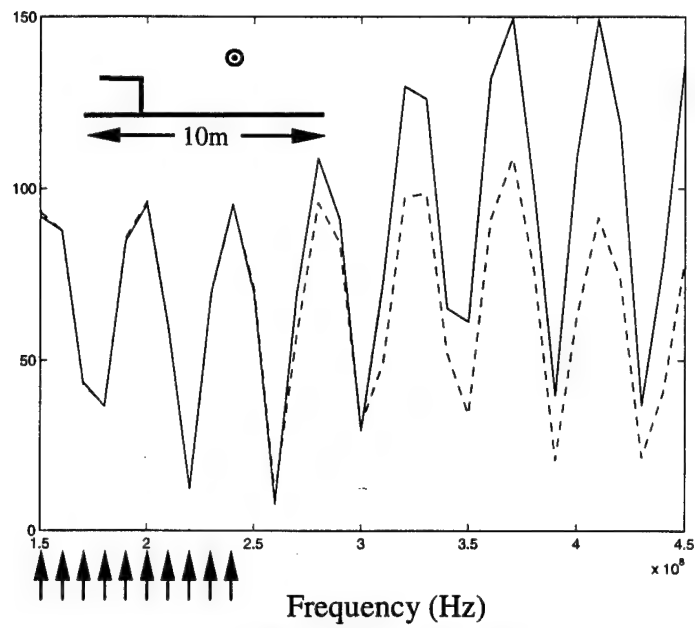
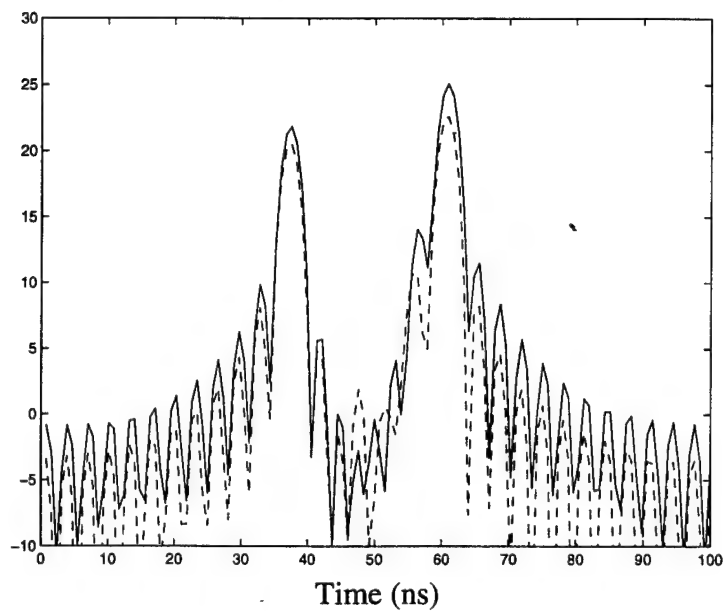


Fig. 1. Time-of-arrival model



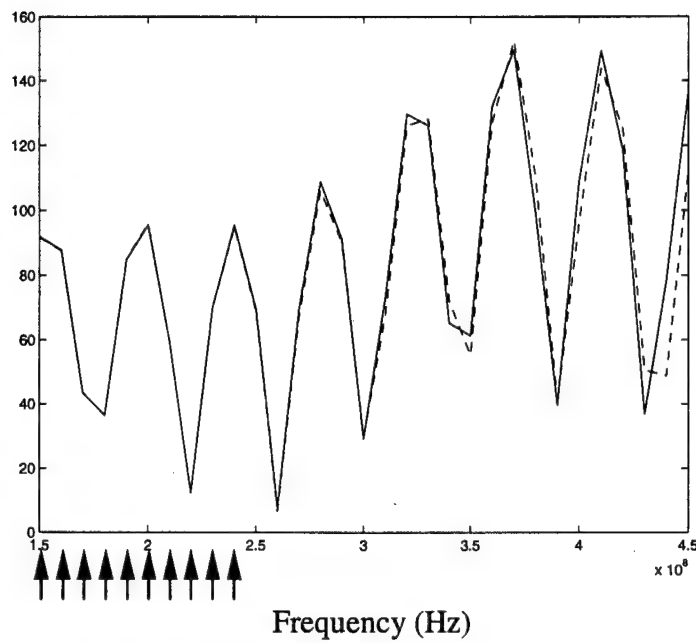
(a) Frequency response



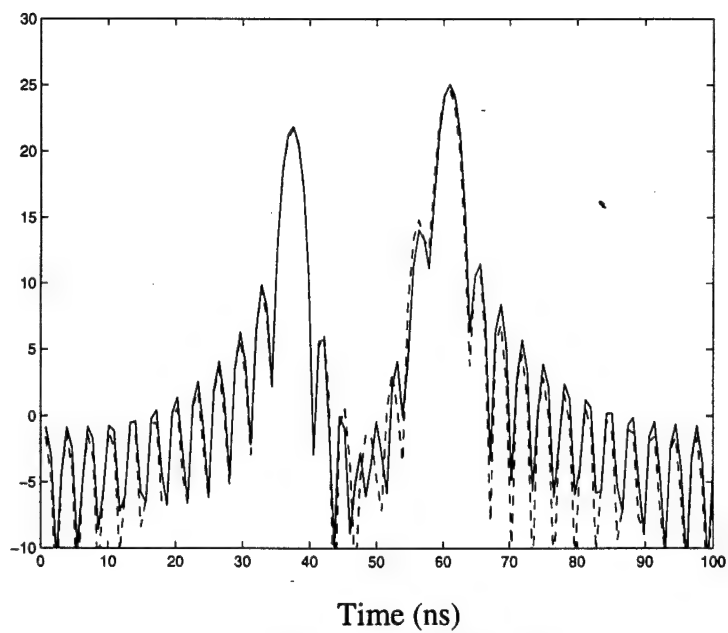
(b) Time domain response

Fig. 2. Frequency extrapolation for 2-D problem (H-Pol). — MoM,  
 ----- 10 point MoM + extrapolation



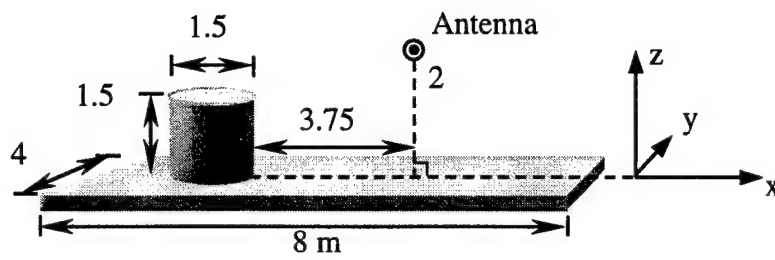


(a) Frequency response

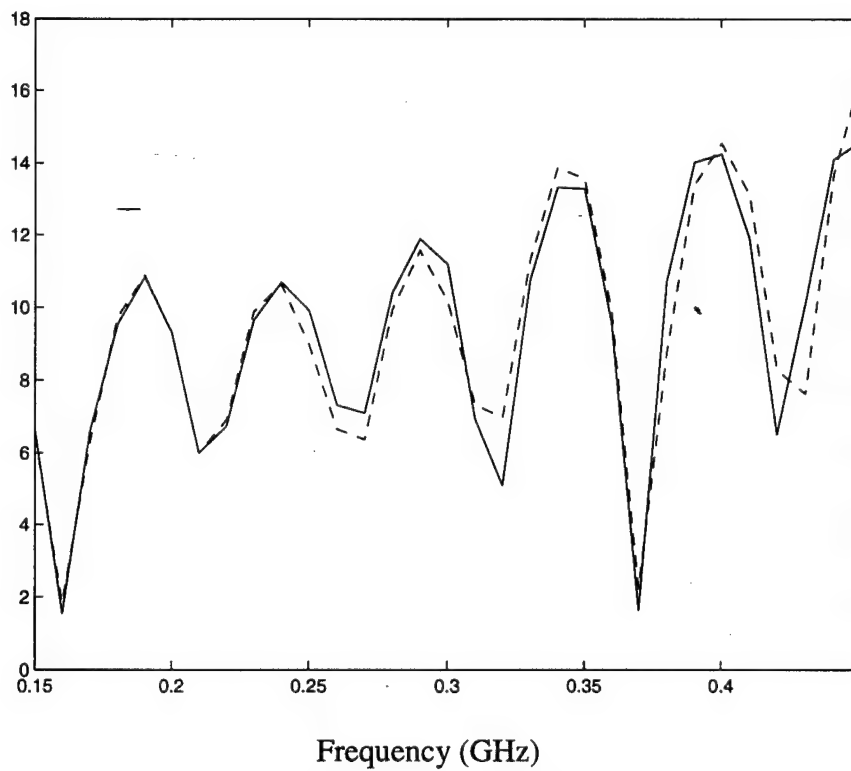


(b) time domain response

Fig. 3. Frequency compensated extrapolation (H-pol).  
 — MoM,  
 ----- 10 point MoM + extrapolation



(a) Geometry of the 3-D platform



(b) Frequency response

Fig. 4. Frequency extrapolation for 3-D radiation. — FISC  
 ----- FISC at 10 point + extrapolation

## Frequency Extrapolation and Model-Based Parameterization of Antenna-Platform Radiation

Tao Su\*, Yuanxun Wang and Hao Ling  
Department of Electrical and Computer Engineering  
The University of Texas at Austin  
Austin, TX 78712

### I. Introduction

The characterization of radiation from a complex platform is usually very time consuming, since the computation complexity of the rigorous solution of a radiation problem grows dramatically as frequency goes high. On the other hand, a broad bandwidth and a high center frequency are usually required in order to characterize the radiation features of the platform. In this paper, we present a frequency extrapolation technique for the antenna radiation problem to obtain the radiated field over a wide band of frequencies. A radiation center representation of the platform is then found from the extrapolated data.

We start with a CAD model of the platform. First, the induced current on the surface is computed using the method of moments (MoM) at a set of low frequencies. A time-of-arrival model is then applied to each current element and the super-resolution algorithm ESPRIT [1] is used to calculate the model coefficients. The frequency response of the current is extrapolated based on this model and the radiated field is obtained over a wide band of frequencies. Next, we assume the radiation can be approximated by the radiation of a set of radiation centers. We estimate the locations of the radiation centers by generating a Antenna Synthetic Aperture Radar (ASAR) [2] image, which is simply an Inverse Fourier Transform of the radiated field. Fine positions of each radiation center is found using match pursuit technique and the radiation centers are extracted one after another until the remaining energy is small enough to be ignored. Thus we come to a radiation center representation of the original radiation problem.

Results show that the frequency extrapolation is quite accurate and the computation time is saved considerably. The radiation center model characterizes most radiation features of the platform. It gives a sparse representation of the radiation problem and is very useful in analysis and design problems.

### II. Methodology

At the beginning of the process, we compute the induced current at a few low frequencies using MoM, using a CAD model as the one in Fig. 1. We assume that the total current is induced by different scattering mechanisms [3][4]. Each of the incident mechanism has a distinct arrival time. Also taking into account the fact that the amplitude of the radiated field from a dipole source is proportional to the frequency, a current element can be written as

$$J(\omega) = \omega \sum_{n=1}^N a_n e^{-j\omega t_n} \quad (1)$$

where  $\omega$  is the angular frequency,  $N$  is the total number of incident mechanisms,  $a_n$  and  $t_n$  are the amplitude and arrival time of the  $n^{\text{th}}$  incident mechanism, respectively.

The model coefficients  $a_n$  and  $t_n$  are obtained using ESPRIT, which is based on the model that the signal consists of a sum of exponential and additive white noise. Once the model parameters are found, the induced current at higher frequencies can be computed using (1). The radiated field is then easily obtained from the extrapolated current.

We assume that the radiated field can be approximated by the radiation of a set of point radiators. To estimate the location of the radiation centers, we Inverse Fourier Transform the radiated field with respect to the frequency and incident angles to generate an ASAR image. The detail of the ASAR algorithm can be found in [2]. The point with the highest intensity is located in the image and its amplitude and coordinate are determined to serve as an estimation of the strongest radiation center. Then we perform a match pursuit algorithm to find the exact location [5]. Assume a radiation center is close to the estimated point, we can find the radiated field from the radiation center given its location and the position of the antenna by

$$E^s(k, \theta_1, \theta_2) = A e^{-jk r_0} e^{jk(x_0 \sin \theta \cos \phi + y_0 \sin \theta \sin \phi + z_0 \sin \theta)} = A e^{-jk r_0} e^{j(k_x x_0 + k_y y_0 + k_z z_0)} \quad (2)$$

where  $k$  is the wave number,  $(x_0, y_0, z_0)$  is the location of the radiation center. The angles  $\theta_1, \theta_2$  are defined in Fig. 2. By slightly varying the position of the radiation center and subtracting its radiated field from the total field, we can come up with an optimal location that causes the maximum energy reduction. Then, subtract the contribution of this radiation center from the total radiated field and repeat the above process, we are able to obtain a set of radiation centers, until the remaining energy is small enough.

### III. Results

An example of the antenna-platform problem is shown in Fig. 1. The induced current is rigorously computed at the frequencies from 0.15 to 0.24 GHz at an interval of 0.01 GHz. The computation is done by FISC [6], which is a MoM code based on the fast multipole method (FMM). The current is then extrapolated and the radiated field is computed. The extrapolation result is compared with the reference field data, which is also computed by FISC over the frequency band from 0.15 to 0.45 GHz at  $\theta = 50^\circ$  and  $\phi = 0^\circ$ , as shown in Fig. 3(a). The corresponding time domain response is plotted in Fig. 3 (b). The matching between the two is good in both the frequency and time domain.

Next, we extract the radiation centers using the match pursuit algorithm base on the extrapolated field over the range that  $f$  varies from 0.6 to 0.9GHz. The first

10 extracted radiation centers are shown in Fig. 5. As we can observe, most of the radiation centers are located on the surface of the platform as we expected.

The radiated field can be easily reconstructed using the radiation centers. The original radiated field at  $k_z = \pi$  is plotted in Fig 6 (a) as a function of the  $k_x$  and  $k_y$ , where  $k_x$ ,  $k_y$  and  $k_z$  are defined in (2). The field reconstructed from the first 10 radiation centers is shown in Fig 6 (b). The two patterns match well at most of the incident angles. Thus the radiation pattern is efficiently approximated by the radiation center model.

#### IV. Conclusions

We have applied the frequency extrapolation technique to the antenna radiation problem. The radiated field over a wide band of frequencies can be extrapolated efficiently based on the computation result at a few lower frequencies. A radiation center model of the platform can be found by performing the match pursuit algorithm. The model proves effective in approximating the original problem since the radiated field can be accurately reconstructed, with very little computation effort.

#### Acknowledgments

This work is supported by the Office of Naval Research under Contract No. N00014-98-1-0178, and in part by the Air Force MURI Center for Computational Electromagnetics under Contract No. AFOSR F49620-96-1-0025.

#### References

- [1] R. Roy, A. Paulraj and T. Kailath, "ESPRIT – a subspace rotation approach to estimation of parameters of cisoids in noise," *IEEE Trans. Acoust., Speech, Signal Processing*, vol. ASSP-34, pp. 1340-1342, Oct. 1986.
- [2] C. Ozdemir, R. Bhalla, L. C. Trintinalia and H. Ling, "ASAR – antenna synthetic aperture radar imaging," submitted to *IEEE Trans. Antennas Propagat.*
- [3] Y. Wang, H. Ling J. Song and W. C. Chew, "A frequency extrapolation algorithm for FISC," *IEEE Trans. Antennas Propagat.*, vol. 45, pp. 1891-1893, Dec. 1997.
- [4] Y. Wang and H. Ling, "Radar signature prediction using moment method codes via a frequency extrapolation technique," submitted to *IEEE Trans. Antennas Propagat.*, Feb. 1998.
- [5] C. Ozdemir, R. Bhalla, and H. Ling, "A radiation center representation of antenna radiation patterns on a complex platform," submitted to *IEEE Trans. Antennas Propagat.*
- [6] *User's Manual for FISC (Fast Illinois Solver Code)*, Center of Computational Electromagnetics, Univ. of Illinois, Champaign, IL, and DEMACO, Inc., Champaign, IL, Jan. 1997.

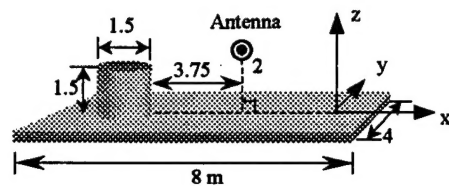


Fig. 1. Geometry of 3-D platform

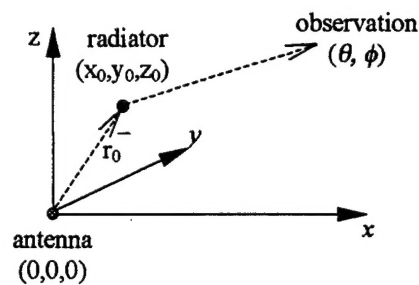
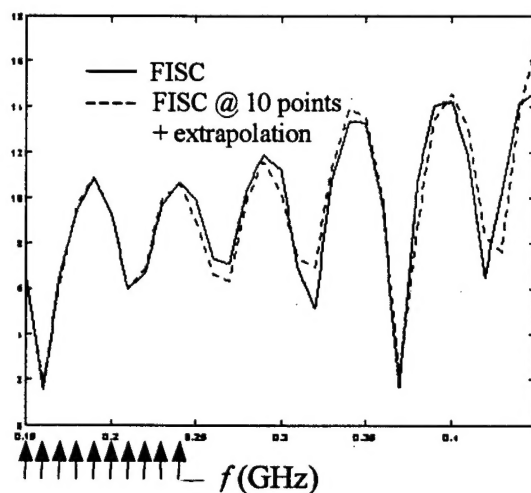
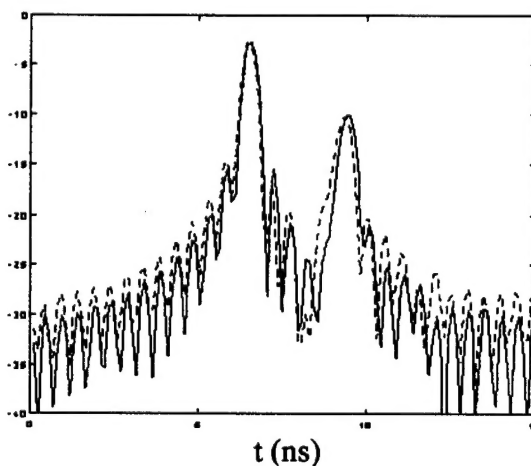


Fig. 2. Radiation center model



(a) Frequency domain response (dB)



(b) Time domain response (dB)

Fig. 3. Frequency Extrapolation

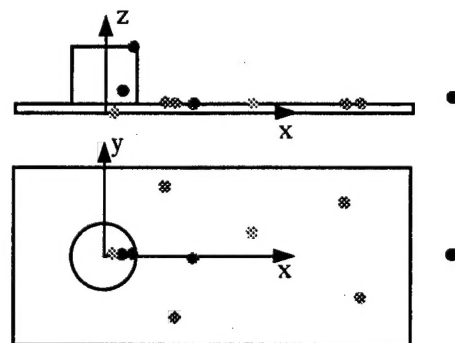
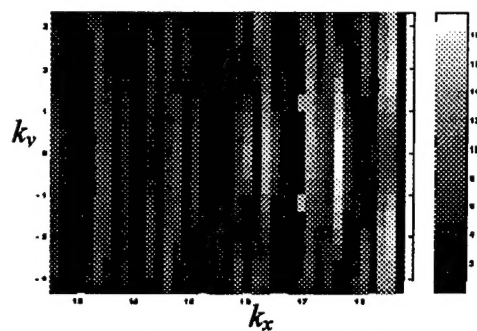
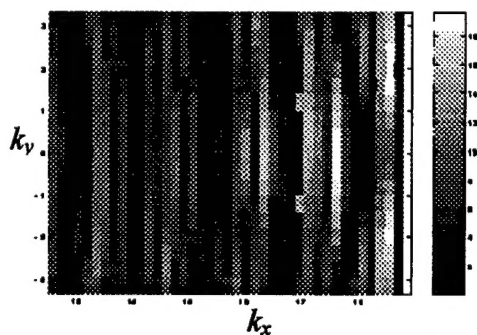


Fig. 4. Extracted radiation centers



(a) Original radiated field



(b) Reconstructed radiated field

Fig. 6. Reconstruction of the radiated field from the radiation center model